RESEARCH ARTICLE | JANUARY 21 2026

Flute instabilities driven by the radial equilibrium flow in a collisional weakly magnetized plasma column

S. Aggarwal ; Y. Camenen ; A. Escarguel ; A. Poyé

Phys. Plasmas 33, 012113 (2026)
https://doi.org/10.1063/5.0300987

Flute instabilities driven by the radial equilibrium flow in a collisional weakly magnetized plasma column

Cite as: Phys. Plasmas **33**, 012113 (2026); doi: 10.1063/5.0300987
Submitted: 5 September 2025 · Accepted: 30 December 2025 ·
Published Online: 21 January 2026

S. Aggarwal,[1,2,a)] Y. Camenen,[3,b)] A. Escarguel,[3] and A. Poyé[3]

AFFILIATIONS

[1]Advanced Research Center for Nanolithography, Science Park 106, 1098 XG Amsterdam, The Netherlands
[2]Department of Physics and Astronomy, and LaserLaB, Vrije Universiteit Amsterdam, De Boelelaan 1081, 1081 HV Amsterdam, The Netherlands
[3]Aix-Marseille Université, CNRS, PIIM UMR 7345, Marseille, France

[a)]**Author to whom correspondence should be addressed:** s.aggarwal@arcnl.nl
[b)]**Electronic mail:** yann.camenen@univ-amu.fr

ABSTRACT

A two-fluid model developed by Aggarwal *et al.* [J. Plasma Phys. **89**, 905890310 (2023)] to study the stability of centrifugal flute modes in a weakly magnetized plasma column is extended to include the impact of the ionization source and the ion–neutral friction force within the ion momentum equation. The model is radially global and applicable for arbitrary perturbation frequency. The dispersion relation takes the form of a third-order differential equation that is solved numerically. The incorporation of an ionization source and friction leads to a finite ion radial equilibrium flow, which brings in an additional drive for instabilities, the other driving factor being the difference between the electron and ion azimuthal flows. The instability mechanisms are discussed, followed by an exploration of the parametric dependencies regarding the growth rate and frequency of the instability. The relative effect of inertia, ionization source, and neutral collisions on the stability of a weakly magnetized plasma column is analyzed. Finally, the model is applied to compute the linear stability of experimentally observed plasmas in the linear plasma column MISTRAL.

I. INTRODUCTION

Low temperature $\mathbf{E} \times \mathbf{B}$ plasmas are used in a variety of applications ranging from Hall thrusters for satellite propulsion,[1–3] ion sources and magnetron discharges for plasma processing,[4,5] and plasma mass separation techniques.[6–8] Numerous intricate physical phenomena witnessed in these devices lack a comprehensive understanding. One of the important issues is the presence of instabilities, which can lead to turbulent transport and affect the performance of the device. In linear magnetized plasma devices, instabilities arise from a variety of factors, including pressure and temperature gradients, plasma–particle interactions, and the influence of electric and magnetic fields. For example, in a strongly ionized plasma column, where ion–neutral collisions are negligible, a Rayleigh–Taylor-type instability arises due to centrifugal acceleration produced by the $\mathbf{E} \times \mathbf{B}$ drift.[9–12] In a weakly ionized plasma, ion–neutral friction can drive the neutral drag instability, which was investigated by Simon[13] and arises due to charge separation resulting from ion–neutral collisions. This mechanism adds to the destabilization due to centrifugal acceleration, and its relative effect varies with the ion–neutral collision frequency. Ion–neutral collision is a crucial parameter to be considered in the description of weakly ionized and partially magnetized plasmas.

One of the challenges in modeling weakly ionized and partially magnetized plasmas is that the standard approximations used for strongly magnetized plasmas are not valid. For strong magnetization conditions, at least as far as the dynamics perpendicular to the magnetic field is concerned, existing models are derived by means of perturbative expansions in powers of the ratio between the gyroradius (ρ_i) of ion species and any other characteristic length (l) such that $\delta = \rho_i/l \ll 1$.[9,10,14–17] This expansion, which helps in obtaining simple models, is definitely not applicable to weakly magnetized plasma systems, for which the electrons are strongly magnetized, whereas ions are weakly magnetized. In addition, the low-frequency expansion,

where the characteristic frequencies are considered small compared to the gyrofrequency of the species under consideration, is routinely performed in strongly magnetized plasmas but is inapplicable to weakly magnetized systems. The case of non-magnetized ions and magnetized electrons is comparatively simpler and has been reviewed recently.[18]

There is a notable scarcity of models that simultaneously consider the impact of weak magnetization on charged species and incorporate interactions between neutrals and charged particles. The few existing models often rely on the low-frequency and local approximation.[19,20] One of the primary reasons for the lack of models considering weak magnetization and neutral collisions is the added complexity that these effects introduce. Additionally, the majority of theoretical approaches rely on local description, i.e., by considering the perturbations to be localized at a single radial location, within the confines of a slab geometry. When comparing these theoretical results with cylindrical experiments, one often establishes a correspondence between Cartesian coordinates and cylindrical coordinates: $x \rightarrow r$ and $y \rightarrow \theta$. The results of the non-local analysis can differ significantly from those obtained through local analysis or analysis in simplified geometries like slab geometry. Neglecting non-local effects can lead to an incomplete or even incorrect understanding of the plasma system, potentially leading to inaccurate predictions or models.[21–23]

To overcome these limitations, Aggarwal *et al.*[23] have developed a model valid at arbitrary frequency and revisited the characteristic features of centrifugal instability and its control in weakly magnetized plasma systems. However, the linear model presented by Aggarwal *et al.*[23] did not include ion–neutral collisions, which can be of significant importance in weakly ionized plasma systems. The present work extends the model presented in Ref. 23 by taking into account the ion–neutral collisions and the ionization source, together with the resulting ion radial flow. The model assumptions are supported by measurements on the magnetized plasma column MISTRAL, a canonical configuration for studying instabilities in cross-field plasmas, where the $\mathbf{E} \times \mathbf{B}$ plasma rotation due to the mean radial electric field E_r is prone to trigger flute modes.[24–29] The formation of coherent rotating structures (sometimes called spokes) in MISTRAL is supposed to be seeded by instabilities. Drift waves, Rayleigh–Taylor/Centrifugal instability, Kelvin–Helmholtz instability, and neutral drag instability have been identified as potential contributors to the formation of these rotating structures. However, a definitive understanding of which instabilities are accountable for their emergence and the specific triggers involved remains elusive. The goal of this study is to improve our understanding of the instabilities that arise in linear plasma columns such as MISTRAL.

The paper is structured as follows: in Sec. II, a brief introduction to the MISTRAL plasma column is given along with the range of experimentally accessible parameters. In Sec. III, the equations and assumptions on which the model is based are provided. In Sec. IV, the linearized equations describing the equilibrium and the first-order perturbations are presented. The dispersion relation is then derived in Sec. V. Section VI presents the linear stability analysis, which includes a description of the instability mechanism and an analysis of the parametric dependency of the instability's growth rate and frequency. The model is then applied to predict the linear stability of MISTRAL plasmas in Sec. VI C. Finally, the summary and conclusions of this work are presented in Sec. VII.

II. MISTRAL EXPERIMENT

MISTRAL is a magnetized linear plasma device (Fig. 1) in which a plasma is produced through the injection of primary electrons emitted from hot tungsten filaments in a linear cylindrical chamber of $r_b = 10$ cm radius, connected to the ground and referred to as the study chamber. The plasma state can be controlled through two biasing grids situated at the entrance and the end of the study chamber. In Fig. 1, these grids are labeled as the separating grid and the collecting grid, respectively. A magnetic field of 10–36 mT is imposed through the magnetic coils surrounding the linear column in which the plasma is produced. MISTRAL offers a broad range of achievable plasma parameters, including electron density (n_e) in the range of 10^{14}–$10^{16}\mathrm{m}^{-3}$, electron temperature (T_e) spanning from 2 to 6 eV, and ion temperature (T_i) of ~0.2 eV. For a complete description of the experiment, the reader is referred to Refs. 25, 29, and 30. Plasma parameters obtained in the MISTRAL experiment serve as a reference point for the theoretical analysis performed in this study.

Typical radial profiles of the electron density (n_e) and plasma potential (ϕ_0) measured using a Langmuir probe in the MISTRAL experiment are shown in Fig. 2. These profiles were obtained in a configuration where both the separating and collecting grids are connected and polarized at −30 V, for an Ar plasma, with an Ar gas pressure, $\mathrm{P} = 2.6 \times 10^{-4}$ mbar, and an axial magnetic field, B = 160 G.[30] In this configuration and for the magnetic field and pressure scans investigated in this work, MISTRAL plasmas exhibit a spoke ($m = 1$ overdense region) rotating azimuthally with a frequency comparable to the ion cyclotron frequency. The profiles shown in Fig. 2 are time-averaged over several periods of the rotating spoke.

The time-averaged electron density and plasma potential profiles are well described by a Gaussian and parabolic profiles, respectively,

$$n_0(r) = n_{00} \exp\left(-\frac{r^2}{r_0^2}\right); \quad \phi_0 = p_1 r^2 + p_2, \tag{1}$$

where r represents the radial coordinate and n_{00}, r_0, p_1, and p_2 are parameterization constants. The parameter r_0 sets the width of the

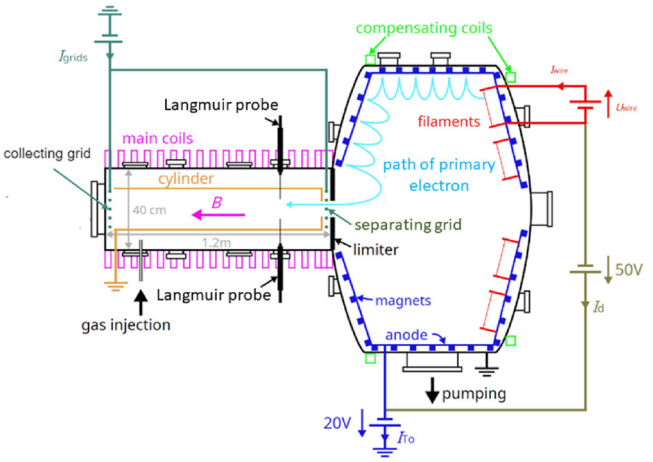

FIG. 1. Schematic of the MISTRAL experiment. Reproduced with permission from S. Aggarwal, "Linear stability of a weakly magnetized rotating plasma column," Ph.D. thesis (Aix-Marseille University, 2023).[30]

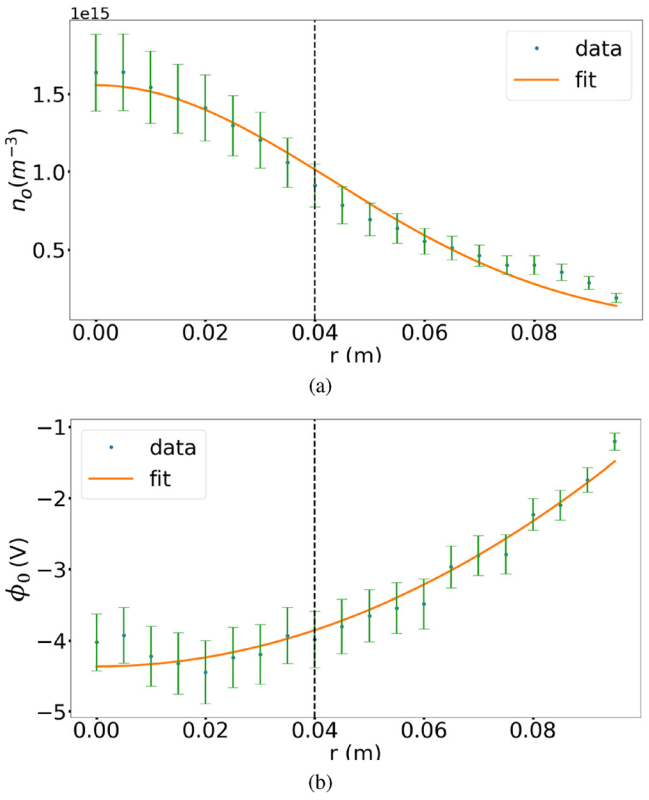

FIG. 2. Time-averaged (a) electron density (n_0) and (b) plasma potential (ϕ_0), as a function of the radial position r for an Ar plasma with both the separating and collecting grids connected and polarized at −30 V. The green points are the experimental measurements, and the orange lines are the fits performed using Eq. (1). The dashed line indicates the position of the limiter.

Gaussian used to describe the density profile. It is representative of the minor radius of the plasma.

Section III presents the model development for investigating the instabilities in the MISTRAL plasma. Motivated by the experimental observations, the background density profile will be assumed to have a Gaussian shape, and the background electric potential to have a parabolic shape.

III. MODEL EQUATIONS

The model describes a cylindrical plasma column bounded radially and immersed in a uniform magnetic field such that $\mathbf{B} = B\hat{e}_z$, see Fig. 3. The continuity equation for species j, where $j = i, e$ denotes either ions or electrons, is

$$\frac{\partial n_j}{\partial t} + \nabla \cdot (n_j \mathbf{v}_j) = S_{ion}. \tag{2}$$

Here, S_{ion} is the ionization source term, n_j is the density of the species, $\mathbf{v}_j$ is the velocity of the species, and m_j is the mass of the species. The ion and electron momentum equations are given by

$$n_i m_i \left(\frac{\partial \mathbf{v_i}}{\partial t} + \mathbf{v_i} \cdot \nabla \mathbf{v_i} \right) = n_i e(-\nabla\phi + \mathbf{v_i} \times \mathbf{B}) - T_i \nabla n_i - m_i n_i \nu_{in} \mathbf{v}_i - m_i S_{ion} \mathbf{v_i}, \tag{3}$$

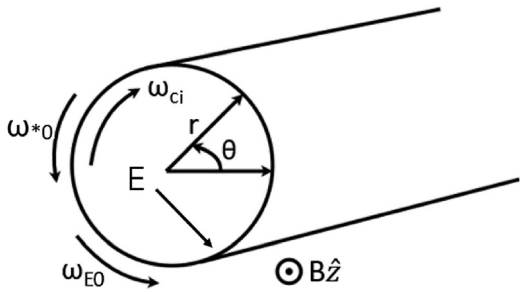

FIG. 3. Cylindrical coordinate system and direction of rotation for ion cyclotron frequency ω_{ci}, positive $E \times B$ frequency ($\omega_{E0} > 0$), and positive diamagnetic frequency ($\omega_{*0} > 0$). Reproduced with permission from Aggarwal *et al.*, "Centrifugal instability in a weakly magnetized rotating plasma column," J. Plasma Phys. **89**, 905890310 (2023). Copyright 2023 Cambridge University Press.[23]

$$0 = -en_e(-\nabla\phi + \mathbf{v}_e \times \mathbf{B}) - \nabla(n_e T_e). \tag{4}$$

In Eqs. (3) and (4), $T_{i,e}$ is the species temperature, ϕ being the electric potential, and ν_{in} being the ion–neutral collision frequency. In the case of MISTRAL, where the ions and secondary electrons are created by ionization from primary electrons produced by the tungsten filaments through collision processes, the ionization source can be written as $S_{ion} = n_{ep}\nu_{ion}$ with n_{ep} as the primary electron density and ν_{ion} as the ionization frequency. The term $m_i S_{ion}\mathbf{v_i}$ in the ion momentum equation represents a sink term due to the ionization of neutrals. The neutrals are assumed to be at rest and have a uniform density since the ionization fraction in MISTRAL plasmas is typically less than 1%. In the ion momentum equation, the off-diagonal terms of the pressure tensor are responsible for finite Larmor radius (FLR) effects and should be retained for a complete description of a magnetized plasma. For strongly magnetized plasmas, approximate closures for the gyroviscosity tensor can be found in the references by Braginskii[31] and Ramos.[32] These works provide foundational formulations of gyroviscous effects in collisional and collisionless regimes, which have been widely used to model plasma transport phenomena. However, no closed form of the gyroviscosity tensor has, to the best of our knowledge, been derived for arbitrary frequencies and Larmor radii, which is the focus of this paper. We therefore neglect this term and will consider later an *ad hoc* cutoff in the radial and azimuthal scales to partly account for finite Larmor radius effects. In the electron momentum equation, inertial effects have been neglected since $m_e/m_i \ll 1$. Coulomb collisions and collisions of electrons with neutrals are neglected as the order of magnitude of these collision frequencies is found to be negligible in comparison to the respective cyclotron frequencies in MISTRAL.[23,30,33] This set of equations is similar to that derived in Ref. 23, except that ion–neutral friction ν_{in} and ionization S_{ion} are retained.

To solve Eqs. (2)–(4), additional assumptions are made: The plasma is considered to be electrostatic ($\frac{\partial \mathbf{B}}{\partial t} = 0$) and quasi-neutral ($n_i = n_e$, $\Delta\phi = 0$). The ion temperature, T_i, is assumed to be radially uniform, consistent with laser-induced fluorescence measurements in MISTRAL,[34] and variations in the axial direction are neglected ($k_{||} = 0$). The assumption $k_{||} = 0$ is motivated by measurements in MISTRAL, showing that in the presence of a rotating spoke, the plasma fluctuations are axially constant, i.e., $k_{||} \ll 2\pi/L$, where L is the length of the plasma column.[35,36]

In cylindrical coordinates, the gradient operator is given by

$$\nabla = \hat{e}_r \frac{\partial}{\partial r} + \hat{e}_\theta \frac{1}{r}\frac{\partial}{\partial \theta} + \hat{e}_z \frac{\partial}{\partial z}, \tag{5}$$

where $\hat{e}_r$, $\hat{e}_\theta$, and $\hat{e}_z$ are the unit vectors in r, θ, and z directions, respectively, see Fig. 3.

IV. LINEARIZED PLASMA EQUATIONS

To obtain the dispersion relation, Eqs. (2)–(4) are linearized. The dependent variables, i.e., plasma density, flow, and electric potential, are written as the sum of a time-independent equilibrium part denoted by subscript 0 and a perturbed part denoted by superscript $\sim$ such that

$$\begin{aligned} n &= n_0 + \tilde{n} \quad \text{and} \quad \tilde{n} = n_1(r)\ \exp[i(m\theta - \omega t)], \\ \mathbf{v} &= \mathbf{v}_0 + \tilde{\mathbf{v}} \quad \text{and} \quad \tilde{\mathbf{v}} = \mathbf{v}_1(r)\ \exp[i(m\theta - \omega t)], \\ \phi &= \phi_0 + \tilde{\phi} \quad \text{and} \quad \tilde{\phi} = \phi_1(r)\ \exp[i(m\theta - \omega t)]. \end{aligned} \tag{6}$$

Here, n_0 represents the equilibrium density of ions or electrons, ϕ_0 is the equilibrium electric potential, and $\mathbf{v}_0$ represents the equilibrium flow. The profiles of n_0 and ϕ_0 are assumed to be Gaussian and parabolic, respectively, see Eq. (1), consistent with the experimental observations. These equilibrium density and potential profiles imply a background rigid body rotation, as will be described in Sec. IV A.

Regarding the perturbed part, $n_1(r)$ and $\phi_1(r)$ represent the amplitudes of the density and potential perturbations, respectively. The perturbed velocity is given by $\mathbf{v}_1(r) = v_{r_1}\hat{e}_r + v_{\theta_1}\hat{e}_\theta$, where v_{r_1} and v_{θ_1} are the radial and azimuthal components of the perturbed velocity, respectively. The azimuthal mode number is denoted as m, and the perturbation frequency, which is a complex number, is expressed as $\omega = \omega_r + i\gamma$ with ω_r representing the real part of the perturbation frequency, also called the mode frequency, and γ being the growth rate of the associated mode number m. The positive frequency corresponds to propagation in the θ direction, see Fig. 3.

Using the decomposition presented in Eq. (6), the equilibrium flow for ions and electrons is first derived in Sec. IV A followed by the linear response of electrons and ions in Secs. IV B and IV C, respectively.

A. Equilibrium description

The description of the equilibrium flow for ions and electrons, including ion–neutral friction, can be found in Ref. 23. This section will focus on recalling the primary outcomes. The equilibrium flow of ions is written in terms of its radial and azimuthal components

$$\mathbf{v_{i0}}(r) = v_{ir_0}\hat{e}_r + v_{i\theta_0}\hat{e}_\theta. \tag{7}$$

Rigid body rotation is assumed such that $v_{i\theta_0} = r\omega_0$ with $\omega_0' = \omega_0'' = 0$, where $'$ represents $\partial/\partial r$ and $''$ represents $\partial^2/\partial r^2$. Solving the zeroth-order part of the ion momentum equation and then projecting it along $\hat{e}_r$, the equilibrium radial ion flow is given by

$$\bar{v}_{ir_0} = \frac{-\bar{\nu}_{eff}\bar{r}\bar{\omega}_0}{1+2\bar{\omega}_0} = -\bar{r}\varepsilon, \tag{8}$$

where $\bar{\nu}_{eff} = \bar{\nu}_{in} + \bar{\mu}$ is the effective frequency due to both ion–neutral collisions and ionization with $\bar{\mu} = S_{ion}/(n_0\omega_{ci}) = \bar{n}_{ep}\bar{\nu}_{ion}$. Quantities with an overbar are normalized quantities. The normalizations used in the model are listed in Table I. When $\bar{\nu}_{eff} = 0$, there is no radial equilibrium flow. For a finite ion–neutral friction and ionization source, the radial flow increases linearly with the minor radius. An ion radial flow parameter, independent of the minor radius, is introduced as

$$\varepsilon = -\frac{\bar{v}_{ir_0}}{\bar{r}} = \frac{\bar{\nu}_{eff}\bar{\omega}_0}{1+2\bar{\omega}_0}. \tag{9}$$

Using Eq. (8) in Eq. (3) and projecting along $\hat{e}_\theta$, the azimuthal ion flow frequency $\bar{\omega}_0 = \bar{v}_{i\theta_0}/\bar{r}$ is

$$\bar{\omega}_0 = \pm\frac{1}{2}\sqrt{\frac{1}{2}\left[b + \sqrt{b^2 + 4\bar{\nu}_{eff}^2}\right]} - \frac{1}{2}, \tag{10}$$

where $b = 1 + 4(\bar{\omega}_{*0} + \bar{\omega}_{E0}) - \bar{\nu}_{eff}^2$. For a complete solution and description of Eq. (10), one can refer to Refs. 37 and 23. For the ion equilibrium flow, the only difference compared to Ref. 23 is that we have retained the ionization source. In practice, this means that $\bar{\nu}_{in}$ is replaced by $\bar{\nu}_{eff} = \bar{\nu}_{in} + \bar{\mu}$.

Here, ω_{E0} is the $\mathbf{E}\times\mathbf{B}$ drift frequency

$$\omega_{E0} = \frac{\mathbf{B}\times\nabla\phi_0}{rB^2}\cdot\hat{e}_\theta = \frac{\phi_0'}{rB}, \tag{11}$$

and ω_{*0} is the ion diamagnetic drift frequency

$$\omega_{*0} = \frac{T_i}{en_0B}\frac{\mathbf{B}\times\nabla n_0}{rB}\cdot\hat{e}_\theta = -\frac{T_i}{erB}\frac{1}{L_n}, \tag{12}$$

with $1/L_n = -n_0'/n_0$ the logarithmic density gradient. For a parabolic density profile and a Gaussian electric potential profile, as given by Eq. (1), ω_{E0} and ω_{*0} are independent of r, since $1/L_n = 2r/r_0^2$, and therefore consistent with the assumption of rigid body rotation. Once normalized, following the conventions summarized in Table I, the diamagnetic drift frequency is given by:

$$\bar{\omega}_{*0} = -\frac{1}{\bar{r}\bar{L}_n}. \tag{13}$$

Writing the equilibrium flow velocity for electrons as

$$\mathbf{v_{e0}} = v_{er_0}\hat{e}_r + v_{e\theta_0}\hat{e}_\theta. \tag{14}$$

Equation (4) is solved directly to get

$$\bar{v}_{er_0} = 0; \quad \bar{v}_{e\theta_0} = \bar{r}\bar{\omega}_{0e} \quad \text{and} \quad \bar{\omega}_{0e} = \bar{\omega}_{E0} + \bar{\omega}_{*e}, \tag{15}$$

TABLE I. Normalized parameters and their definitions. Here, $T_{e0_{ref}}$ is the reference value of the electron temperature, and the following definitions are used: $\rho_i = v_{thi}/\omega_{ci}$, $\omega_{ci} = eB/m_i$, and $v_{thi} = \sqrt{T_i/m_i}$. Reproduced with permission from Aggarwal *et al.*, "Centrifugal instability in a weakly magnetized rotating plasma column," J. Plasma Phys. **89**, 905890310 (2023). Copyright 2023 Cambridge University Press.[23]

Variable	Notation	Definition
Normalized frequencies	$\bar{\nu}, \bar{\omega}$	$\nu/\omega_{ci}, \omega/\omega_{ci}$
Normalized lengths	$\bar{r}, 1/\bar{L}_n$	$r/\rho_i, \rho_i/L_n$
Normalized perturbed density	$\bar{n}_1, \bar{n}_{ep}$	$n_1/n_0, n_{ep}/n_0$
Normalized perturbed potential	$\bar{\phi}_1$	$e\phi_1/T_{e0_{ref}}$
Normalized velocities	$\bar{v}_{i,e}$	$v_{i,e}/v_{thi}$

where $\bar{\omega}_{0e}$ is the electron equilibrium flow frequency and $\bar{\omega}_{*e}$ is the electron diamagnetic drift frequency ω_{*e} normalized to the ion cyclotron frequency with

$$\omega_{*e} = -\frac{1}{en_0 B}\frac{\mathbf{B}\times\nabla(n_0 T_{e0})}{rB}\cdot\hat{e}_\theta. \tag{16}$$

The range of characteristic frequencies observed in MISTRAL as a function of pressure and magnetic field is shown in Fig. 4. The frequencies are normalized to the ion cyclotron frequency ω_{ci}, which confirms that the ordering $\omega/\omega_{ci} \ll 1$ is not valid for weakly ionized and weakly magnetized $\mathbf{E}\times\mathbf{B}$ plasmas. The parameters ε and $\bar{\mu}$, which characterize the magnitude of the equilibrium radial flow and the ionization source, respectively, are also displayed as they will be important for the linear analysis as shown in Sec. VI. The experiments and measurements performed to obtain these parameters are described in Sec. II.

After the description of the equilibrium flow, the next step is to obtain the linearized divergence of the ion and electron particle flux, which is done in Sec. IV B.

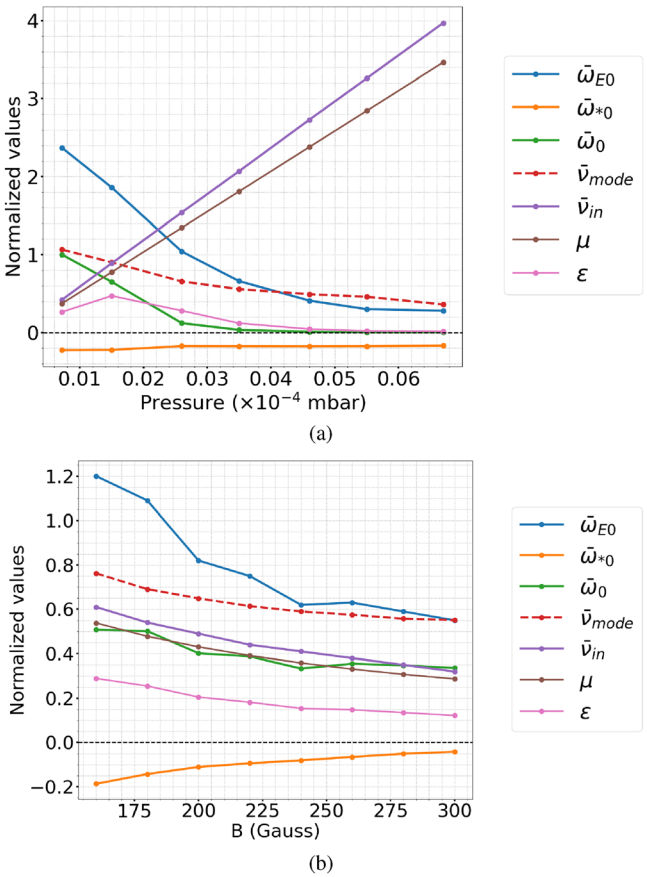

FIG. 4. Normalized $\mathbf{E}\times\mathbf{B}$ drift frequency ($\bar{\omega}_{E0}$), normalized ion diamagnetic drift frequency ($\bar{\omega}_{*0}$), normalized equilibrium flow frequency ($\bar{\omega}_0$), normalized spoke frequency ($\bar{\nu}_{mode}$), normalized ion–neutral collision frequency ($\bar{\nu}_{in}$), and parameters $\bar{\mu}$ and ε as a function of (a) Pressure at B = 160 G and for various values of (b) B at P = 1.04 ×10^{-4} mbar.

B. Linear electron response

Rearranging Eq. (4), the electron flow can be written in the following form:

$$\mathbf{v}_e = \frac{\mathbf{b}\times\nabla\phi}{B} + \frac{1}{en_e}\frac{\mathbf{b}\times\nabla(n_e T_e)}{B}, \tag{17}$$

which is simply the sum of $\mathbf{E}\times\mathbf{B}$ flow and diamagnetic flow. Multiplying Eq. (17) by n_e, taking the divergence on both sides, and then linearizing, one gets

$$\nabla\cdot(n_e\mathbf{v}_e)|_1 = -im\frac{\phi_1}{rB}n_0' + im\omega_{E0}n_1. \tag{18}$$

Using the above equation and replacing $\partial/\partial t$ with $-i\omega$ in the linearized form of the electron continuity equation, Eq. (2), a relationship is established between the normalized perturbed density and potential[10,16,23]

$$\bar{n}_1 = \alpha_*\tau\bar{\phi}_1, \tag{19}$$

where

$$\alpha_* = \frac{m}{\bar{r}\bar{L}_n}\frac{1}{\bar{\omega} - m\bar{\omega}_{E0}}, \tag{20}$$

and where $\tau = T_{e0_{ref}}/T_{io}$ with $T_{e0_{ref}}$ being the value of the electron temperature at $r = 0$.

C. Linear ion response

The linearized ion-momentum equation, Eq. (3), writes

$$\begin{aligned} &-i\omega\mathbf{v}_{i1} + (\mathbf{v}_{i0}\cdot\nabla)\mathbf{v}_{i1} + (\mathbf{v}_{i1}\cdot\nabla)\mathbf{v}_{i0} \\ &= \frac{e}{m_i}[-\nabla\phi + \mathbf{v}_{i1}\times\mathbf{B}] \\ &\quad -\frac{T_i}{m_i}\nabla\frac{n_1}{n_o} - \nu_{in}\mathbf{v}_{i1} - \frac{S_{ion}}{n_0}\left(\mathbf{v}_{i1} - \frac{n_1}{n_0}\mathbf{v}_{io}\right). \end{aligned} \tag{21}$$

Using the expression for $\mathbf{v}_{i0}$, given by Eq. (7), under the rigid body rotation assumption, the inertial terms in the above equation are

$$(\mathbf{v}_{i0}\cdot\nabla)\mathbf{v}_{i1} = [\nu_{ir_0}\mathbf{v}_{i1}' + im\omega_0\mathbf{v}_{i1} - \omega_0(\mathbf{v}_{i1}\times\mathbf{b})], \tag{22}$$

and

$$(\mathbf{v}_{i1}\cdot\nabla)\mathbf{v}_{i0} = [\nu_{ir_0}'\mathbf{v}_{i1} - \omega_0(\mathbf{v}_{i1}\times\mathbf{b})]. \tag{23}$$

Including these terms in the linearized ion-momentum equation, Eq. (21), normalizing the frequencies with ion-cyclotron frequency, lengths with ion-Larmor radius and substituting the value of ν_{ir_0}, Eq. (21) becomes

$$-i\bar{\omega}_c\bar{\mathbf{v}}_{i1} = C(\bar{\mathbf{v}}_{i1}\times\mathbf{b}) - \nabla\Phi_1 + \varepsilon(\bar{r}\bar{\mathbf{v}}_{i1}' + \bar{\mathbf{v}}_{i1}) + \bar{\mu}\bar{n}_1\mathbf{v}_{i0}. \tag{24}$$

Here, ε is the ion radial flow parameter defined in Eq. (9), $C = 1 + 2\bar{\omega}_0$ is the factor by which the Lorentz force is modified due to the inertial force, and $\bar{\omega}_c = \bar{\omega}_{ph} + i\bar{\nu}_{eff}$ with $\bar{\omega}_{ph} = \bar{\omega} - m\bar{\omega}_0$ being the Doppler-shifted frequency. The quantity $\Phi_1 = \bar{n}_1 + \tau\bar{\phi}_1$ has been introduced to make the equations more compact. Once Φ_1 is obtained by solving the final dispersion relation, Eq. (19) can be used to retrieve $\bar{n}_1$ and $\bar{\phi}_1$. For $\bar{\nu}_{eff} = 0$ and $\bar{\mu} = 0$, one recovers the collisionless case as given by Eq. (4.8) in Ref. 23. The term proportional to ε in Eq. (24)

arises from the radial component of the equilibrium flow in the perturbed ion momentum equation, Eq. (3). The term with $\bar{\mu}$ is due to the impact of the ionization source on the background flow.

The expression given by Eq. (19) and the relation $\Phi_1' = \bar{n}_1 + \tau\bar{\phi}_1$ is then used to write $\bar{n}_1$ in terms of Φ_1

$$\bar{n}_1 = \frac{\alpha_*}{1+\alpha_*}\Phi_1 = \lambda\Phi_1, \tag{25}$$

with

$$\lambda = \frac{\alpha_*}{1+\alpha_*} = \frac{m}{\bar{r}\bar{L}_n}\frac{1}{\bar{\omega}_{ph} + m\delta\bar{\omega}_0}, \tag{26}$$

and

$$\delta\bar{\omega}_0 = \bar{\omega}_0 - \bar{\omega}_{E0} - \bar{\omega}_{*0}. \tag{27}$$

Expressing $\bar{n}_1$ in terms of Φ_1 in Eq. (24), a coupled differential equation relating $\bar{\mathbf{v}}_{i1}$ with Φ_1 is obtained

$$(L_1 + L_2)\bar{\mathbf{v}}_{i1} = L_3[\nabla\Phi_1 + \lambda\bar{\mu}(\varepsilon\bar{r}\hat{e}_r - \bar{\omega}_0\bar{r}\hat{e}_\theta)\Phi_1], \tag{28}$$

where L_1, L_2, and L_3 are linear operators

$$\begin{aligned} L_1 &= \left(C^2 - \bar{\omega}_c^2\right) + i\varepsilon\bar{\omega}_c\left(1 + \bar{r}\frac{\partial}{\partial\bar{r}}\right), \\ L_2 &= \varepsilon C\mathbf{b}\times\left(1 + \bar{r}\frac{\partial}{\partial\bar{r}}\right), \\ L_3 &= i\bar{\omega}_c + C\mathbf{b}\times, \end{aligned} \tag{29}$$

with $\mathbf{b} = \mathbf{B}/B$ as the unit vector in the axial direction.

Operating on Eq. (28) first with L_1 and then with L_2, subsequently subtracting the latter equation from the first, noticing that the operators L_1 and L_2 commute ($[L_1, L_2] = 0$), we obtain

$$\begin{aligned} &\left[\left(C^2 - \bar{\omega}_c^2\right)^2 + 2i\varepsilon\bar{\omega}_c\left(C^2 - \bar{\omega}_c^2\right)\left(1 + \bar{r}\frac{\partial}{\partial\bar{r}}\right)\right. \\ &\quad \left. + \varepsilon^2\left(C^2 - \bar{\omega}_c^2\right)\left(1 + \bar{r}\frac{\partial}{\partial\bar{r}}\right)^2\right]\bar{\mathbf{v}}_{i1} \\ &= \left[\left(C^2 - \bar{\omega}_c^2\right)(i\bar{\omega}_c + C\mathbf{b}\times) + \varepsilon\left(C^2 - \bar{\omega}_c^2\right)\left(1 + \bar{r}\frac{\partial}{\partial\bar{r}}\right)\right] \\ &\quad \times [\nabla\Phi_1 + \lambda\bar{\mu}(\varepsilon\bar{r}\hat{e}_r - \bar{\omega}_0\bar{r}\hat{e}_\theta)\Phi_1]. \end{aligned} \tag{30}$$

The equation above is a second-order differential equation relating $\bar{\mathbf{v}}_{i1}$ to Φ_1. For MISTRAL plasmas, the parameter $\varepsilon = \bar{\nu}_{eff}\bar{\omega}_0/C$, characterizing the radial equilibrium ion flow, is observed to be small, i.e., $\varepsilon < 0.3$, see Fig. 4. This is because when the neutral pressure is increased, the electric potential profile flattens, resulting in a lower $\mathbf{E}\times\mathbf{B}$ frequency ω_{E0}, and therefore much smaller ω_0, compensating for the increase in $\bar{\nu}_{eff}$. The experimental observation of $\varepsilon \ll 1$ motivates performing an expansion to the first order in ε to solve Eq. (30) and obtain $\bar{\mathbf{v}}_{i1}$ in terms of Φ_1

$$\bar{\mathbf{v}}_{i1} = \bar{\mathbf{v}}_{i1}^{(0)} + \varepsilon\bar{\mathbf{v}}_{i1}^{(1)}, \tag{31}$$

where $\bar{\mathbf{v}}_{i1}^{(0)}$ is the ion fluid velocity when $\varepsilon = 0$. Using this expansion in Eq. (30), the zeroth-order component $\bar{\mathbf{v}}_{i1}^{(0)}$ is

$$\bar{\mathbf{v}}_{i1}^{(0)} = \frac{C}{C^2 - \bar{\omega}_c^2}\left[\mathbf{b}\times\nabla\Phi_1 + \frac{i\bar{\omega}_c}{C}\nabla\Phi_1 - \lambda\bar{\mu}\left(\frac{i\bar{\omega}_c}{C}\hat{e}_\theta - \hat{e}_r\right)\bar{r}\bar{\omega}_0\Phi_1\right].$$

This expression is similar to that obtained for the collisionless case given by Eq. (4.14) in Ref. 23 with additional terms proportional to $\bar{\mu}$ due to the presence of an ionization source and with $\bar{\omega}_{ph}$ replaced by $\bar{\omega}_c = \bar{\omega}_{ph} + i\bar{\nu}_{eff}$. The first-order component $\bar{\mathbf{v}}_{i1}^{(1)}$ is

$$\begin{aligned} \bar{\mathbf{v}}_{i1}^{(1)} = &\frac{C^2 + \bar{\omega}_c^2}{\left(C^2 - \bar{\omega}_c^2\right)^2}\left[\left(\Phi_1'\hat{e}_r + \bar{r}\nabla\Phi_1'\right) - \frac{2iC\bar{\omega}_c}{C^2 + \bar{\omega}_c^2}\mathbf{b}\times\left(\Phi_1'\hat{e}_r + \bar{r}\nabla\Phi_1'\right)\right] \\ &- \lambda\bar{\mu}\frac{C^2 + \bar{\omega}_c^2}{\left(C^2 - \bar{\omega}_c^2\right)^2}\left[\left(\hat{e}_\theta + \frac{2iC\bar{\omega}_c}{C^2 + \bar{\omega}_c^2}\hat{e}_r\right)\left(2\Phi_1 + \bar{r}\Phi_1'\right)\bar{r}\bar{\omega}_0\right. \\ &\left. - \bar{r}\Phi_1\left(\frac{C^2 - \bar{\omega}_c^2}{C^2 + \bar{\omega}_c^2}\right)(i\bar{\omega}_c\hat{e}_r + C\hat{e}_\theta)\right]. \end{aligned} \tag{32}$$

The next step is to compute the linearized divergence of the ion particle flux

$$\nabla\cdot(n_i\bar{\mathbf{v}}_i)|_1 = n_0\nabla\cdot\bar{\mathbf{v}}_{i1} + \bar{\mathbf{v}}_{i1}\cdot\nabla n_0 + n_1\nabla\cdot\bar{\mathbf{v}}_0 + \bar{\mathbf{v}}_0\cdot\nabla n_1. \tag{33}$$

Expanding Eq. (33) in terms of $\bar{\mathbf{v}}_{i1}^{(0)}$ and $\bar{\mathbf{v}}_{i1}^{(1)}$, we get

$$\begin{aligned} \nabla\cdot(n_i\bar{\mathbf{v}}_i)|_1 = &n_0\nabla\cdot\bar{\mathbf{v}}_{i1}^{(0)} + \bar{\mathbf{v}}_{i1}^{(0)}\cdot\nabla n_0 \\ &+ \varepsilon\left(n_0\nabla\cdot\bar{\mathbf{v}}_{i1}^{(1)} + \bar{\mathbf{v}}_{i1}^{(1)}\cdot\nabla n_0\right) \\ &+ n_1\nabla\cdot\bar{\mathbf{v}}_{i0} + \bar{\mathbf{v}}_{i0}\cdot\nabla n_1. \end{aligned} \tag{34}$$

Compared to the collisionless case, the presence of ion–neutral friction and ionization source terms introduces a finite radial equilibrium flow $\bar{\mathbf{v}}_{ir_0}$, leading to terms proportional to ε. The six terms entering Eq. (34) are detailed in Appendix A.

V. DISPERSION RELATION

Once the divergence of the linearized ion and electron flux is computed, the dispersion relation is obtained by combining quasi-neutrality ($n_e = n_i$) with the continuity equation

$$\nabla\cdot(n_e\mathbf{v}_e)|_1 = \nabla\cdot(n_i\mathbf{v}_i)|_1. \tag{35}$$

After a few additional steps detailed in Appendix A, the dispersion relation is given by

$$\begin{aligned} &\varepsilon\Phi_1''' + \left[\frac{C_{NC}}{\bar{r}} + \varepsilon\left(\frac{3}{\bar{r}} - \frac{1}{\bar{L}_n}\right) - i\bar{\omega}_0 a\lambda\bar{\mu}\varepsilon\bar{r}\right]\Phi_1'' \\ &+ \left[\frac{C_{NC}}{\bar{r}}\left(\frac{1}{\bar{r}} - \frac{1}{\bar{L}_n}\right) + \varepsilon\left(-\frac{m^2}{\bar{r}^2} + \frac{1}{\bar{r}}\left(\frac{1}{\bar{r}} - \frac{1}{\bar{L}_n}\right) + a\frac{m}{\bar{r}\bar{L}_n} - b\lambda\right)\right. \\ &\left. + \frac{\lambda bC\bar{\omega}_0}{\left(C^2 - \bar{\omega}_c^2\right)} - \lambda\bar{\mu}\varepsilon\left(im\bar{\omega}_0 + i\bar{\omega}_0 a\bar{r}\left(\frac{5}{\bar{r}} - \frac{1}{\bar{L}_n}\right) - C_{NC}\right)\right]\Phi_1' \\ &+ \left[\frac{C_{NC}}{\bar{r}}\left(-\frac{m^2}{\bar{r}^2} + \frac{N}{\bar{r}\bar{L}_n}\right) - \varepsilon\lambda b\left(\frac{2}{\bar{r}} - \frac{1}{\bar{L}_n}\right)\right. \\ &+ \frac{\lambda\bar{\mu}C\bar{\omega}_0 b}{\left(C^2 - \bar{\omega}_c^2\right)}\left(\frac{m\bar{\omega}_c}{\bar{r}C} + \frac{2}{\bar{r}} - \frac{1}{\bar{L}_n}\right) \\ &- \lambda\bar{\mu}\varepsilon\left(\frac{2im\bar{\omega}_0}{\bar{r}} + 2i\bar{\omega}_0 a\left(\frac{2}{\bar{r}} - \frac{1}{\bar{L}_n}\right) - \frac{imCb}{\bar{r}\left(C^2 - \bar{\omega}_c^2\right)}\right. \\ &\left.\left. - C_{NC}\left(\frac{2}{\bar{r}} - \frac{1}{\bar{L}_n}\right)\right)\right]\Phi_1 = 0, \end{aligned} \tag{36}$$

where

$$\lambda = \frac{\alpha_*}{1+\alpha_*}, \quad a = \frac{2C\bar{\omega}_c}{C^2+\bar{\omega}_c^2}, \quad C_{NC} = i\bar{\omega}_c\left(\frac{C^2-\bar{\omega}_c^2}{C^2+\bar{\omega}_c^2}\right),$$
$$\frac{N}{\bar{r}\bar{L}_n} = -\lambda(C^2-\bar{\omega}_c^2)\frac{\bar{\omega}_{ph}}{\bar{\omega}_c} + \frac{m}{\bar{r}\bar{L}_n}\frac{C}{\bar{\omega}_c}, \quad b = \frac{(C^2-\bar{\omega}_c^2)^2}{C^2+\bar{\omega}_c^2}. \tag{37}$$

All coefficients are independent of $\bar{r}$. The factor $1/\bar{r}\bar{L}_n$ is also independent of $\bar{r}$ since the density profile is assumed to be Gaussian: $1/\bar{r}\bar{L}_n = 2/\bar{r}_0^2$.

The inputs entering Eq. (36) are the logarithmic density gradient $\bar{L}_n$, the ion radial flow parameter ε, the ion azimuthal flow parameter $\bar{\omega}_0$, the inertial force parameter C, the azimuthal flow drive parameter $\delta\bar{\omega}_0$, the effective collisionality $\bar{\nu}_{eff}$, and the ionization source term $\bar{\mu}$. All the inputs can be computed self-consistently using the results of Sec. IV A or using the parameters given in Tables II and III, which gives the equilibrium flow as a function of the $\mathbf{E}\times\mathbf{B}$ flow, diamagnetic flow, collisionality and ionization source, or set independently to investigate specific physical mechanisms.

Once the boundary conditions are specified at $\bar{r}=0$ and $\bar{r}=r_b$, the solution of Eq. (36) yields the eigenfunction Φ_1 with the corresponding eigenfrequency $\bar{\omega}_c = \bar{\omega} - m\bar{\omega}_0 + i\bar{\nu}_{eff}$.

A. Solving procedure

Equation (36) is a third-order differential equation with a regular singularity at $\bar{r}=0$. It is solved using the Cauchy–Euler formalism, as detailed in Appendix C. Two distinct branches are obtained, corresponding to two roots of the indicial equation, namely, m and $\chi = -C_{NC}/\varepsilon$, leading to the following form of the eigenfunction:

$$\Phi_1 = B_1\bar{r}^m\phi_B + C_1\bar{r}^\chi\phi_\chi, \tag{38}$$

where $\phi_B = \sum_{n=0}^{\infty} a_{m,n}\bar{r}^n$ and $\phi_\chi = \sum_{n=0}^{\infty} a_{\chi,n}\bar{r}^n$, B_1 and C_1 are integration constants, and $a_{\alpha,n}$ is the n^{th} term given by the recurrence relation in Eq. (C6), with $\alpha = m$ or χ. The coefficients $a_{\alpha,n}$ are functions of the mode frequency $\bar{\omega} = \bar{\omega}_r + i\bar{\gamma}$. The integration constants are determined by imposing the boundary condition $\Phi_1 = 0$ at $\bar{r}=0$ and $\bar{r}=\bar{r}_b$. The enforcement of zero fluctuations at $\bar{r}=\bar{r}_b$ is motivated by the presence of a grounded conducting wall at the boundary, but alternative boundary conditions that account for sheath physics, for example, are possible and could be explored with the present formalism. At $\bar{r}=0$, Φ_1' is imposed to be finite for $m=1$, and $\Phi_1'=0$ is imposed for $m>1$, for continuity on the column axis. The radial derivative of Φ_1 is

$$\Phi_1' = \sum_{n=0}^{\infty}(m+n)B_1 a_{m,n}r^{m+n-1} + (\chi+n)C_1 a_{\chi,n}r^{\chi+n-1}. \tag{39}$$

Case 1: $\Re(\chi) < 1$

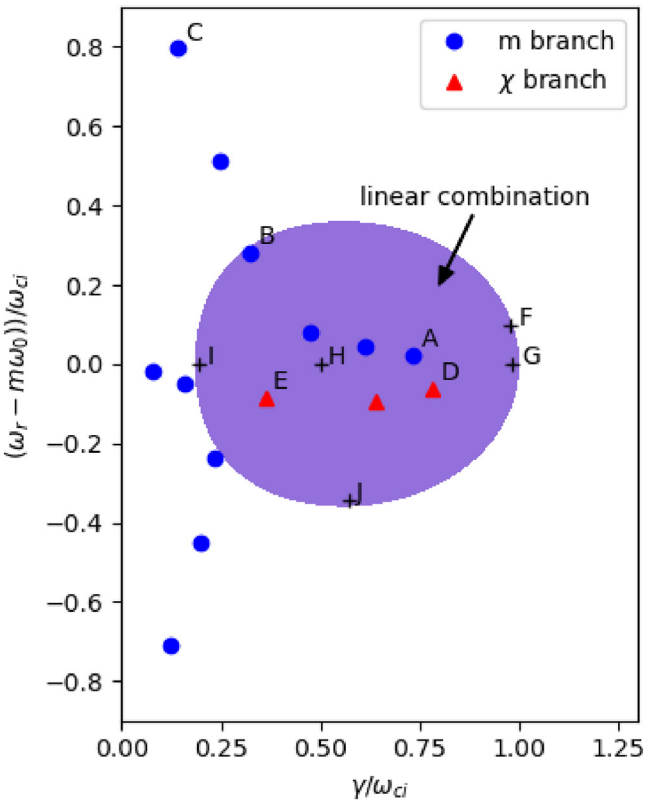

FIG. 5. Solutions of Eq. (36) satisfying the boundary condition $\Phi_1(\bar{r}_b)=0$. The pure m branch is indicated with blue dots, the pure χ branch with red triangles, and the linear combination region with the purple area. The input parameters used in Eq. (36) are $m=1$, $\bar{r}_b=5.54$, $r_0=10/3$, $\varepsilon=0.2$, $\delta\bar{\omega}_0=0$, $\bar{\nu}_{eff}=0$, $\bar{\mu}=0$, $\bar{\omega}_0=0.48$ (obtained from $\bar{\omega}_{E0}=0.9$ and $\bar{\omega}_{*0}=-0.18$), and $C=1$. This ccorrespondsto the case investigated in Sec. VI B.

TABLE II. Characteristic frequencies of MISTRAL plasma for Ar at B = 160 G. All frequencies are normalized to the ion-cyclotron frequency.

P (mbar)	r_0 (cm)	p_1	p_2	$\bar{\omega}_{E0}$	$\bar{\omega}_{*0}$	$\bar{\nu}_{in}$	$\bar{\mu}$	$\bar{\omega}_0$
7.15×10^{-5}	5.36	725.26	−7.88	2.37	−0.22	0.42	0.37	1.001
1.5×10^{-4}	5.41	569.14	−6.4	1.86	−0.22	0.89	0.78	0.65
2.6×10^{-4}	6.1	319.05	−4.37	1.04	−0.18	1.54	1.34	0.12
3.5×10^{-4}	6.07	202.7	−3.39	0.66	−0.18	2.07	1.81	0.03
4.6×10^{-4}	6.05	127.16	−2.78	0.41	−0.18	2.73	2.38	0.01
5.5×10^{-4}	6.08	95.54	−2.43	0.3	−0.18	3.26	2.84	0.003
6.7×10^{-4}	6.22	85.79	−2.24	0.28	−0.17	3.97	3.46	0.002

TABLE III. Characteristic frequencies of MISTRAL plasma for Ar at P = 1.04×10^{-4} mbar. Here, ω_{ci} is in kHz, ρ_i and r_0 are in cm. All other frequencies are normalized to the ion-cyclotron frequency.

B (G)	ω_{ci}	ρ_i	r_0	p_1	p_2	$\bar{\omega}_E$	$\bar{\omega}_{*0}$	$\bar{\nu}_{in}$	$\bar{\mu}$	$\bar{\omega}_0$
160	6.1	1.8	5.89	371.94	−4.15	1.2	−0.19	0.61	0.54	0.51
180	6.86	1.6	5.99	412.95	−4.74	1.09	−0.14	0.54	0.48	0.5
200	7.6	1.4	5.95	394.61	−5.25	0.82	−0.12	0.49	0.43	0.4
220	8.39	1.3	5.99	437.30	−5.83	0.75	−0.1	0.44	0.39	0.38
240	9.15	1.2	5.97	430.87	−6.45	0.62	−0.08	0.41	0.36	0.33
260	9.91	1.11	6.14	512.16	−6.98	0.63	−0.06	0.38	0.33	0.35
280	10.67	1.03	6.46	554.88	−7.52	0.59	−0.05	0.35	0.31	0.34
300	11.44	0.96	6.62	589.12	−8.11	0.55	−0.04	0.32	0.29	0.33

To avoid a diverging Φ_1' at $\bar{r} = 0$, the integration constant C_1 is set to zero. The eigenfunction Φ_1 is then given by

$$\Phi_1 = B_1 \bar{r}^m \phi_B. \tag{40}$$

Case 2: $\Re(\chi) > 1$

The condition $\Phi_1' = 0$ at $\bar{r} = 0$ is always satisfied. Since any multiple of a solution is also a solution, B_1 can be set arbitrarily. For $B_1 \neq 0$, the other integration constant C_1 is chosen to satisfy the boundary condition $\Phi_1(\bar{r}_b) = 0$

$$B_1 \bar{r}_b^m \phi_B(\bar{r}_b) + C_1 \bar{r}_b^\chi \phi_\chi(\bar{r}_b) = 0, \tag{41}$$

leading to the following eigenfunction:

$$\Phi_1 = B_1 \bar{r}^m \phi_B - B_1 \frac{\phi_B(\bar{r}_b)}{\phi_\chi(\bar{r}_b)} \bar{r}_b^{m-\chi} \bar{r}^\chi \phi_\chi. \tag{42}$$

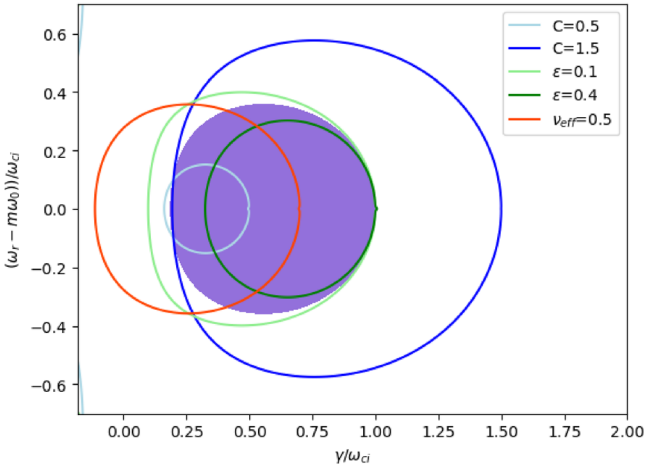

FIG. 6. Boundary of the linear combination region, $\Re(\chi) = 1$, for various values of the parameters C, ε, and $\bar{\nu}_{eff}$.

Case 3: $\Re(\chi) = 1$ and $m > 1$

In this case, it is necessary to set $C_1 = 0$ to satisfy $\Phi_1' = 0$ at $\bar{r} = 0$. The solution is the same as in case 1.

Case 4: $\Re(\chi) = 1$ and $m = 1$

In this case, a finite value of $\Phi_1' =$ is always obtained at $\bar{r} = 0$. The solution is the same as in case 2.

Note that in cases 2 and 4, a solution satisfying $\Phi_1(\bar{r}_b) = 0$ can always be found by adjusting the integration constant C_1 (provided $B_1 \neq 0$). In cases 1 and 3, the boundary condition at $\bar{r} = \bar{r}_b$ is satisfied only for specific values of $(\bar{\gamma}, \bar{\omega}_r)$. Figure 5 shows the location of the solutions for a typical case in the $(\bar{\gamma}, \bar{\omega}_r)$ plane. The pure m branch (cases 1, 3 and cases 2, 4 when $C_1 = 0$) is indicated with blue dots, the pure χ branch (cases 2 and 4 when $B_1 = 0$) with red triangles, and the region where the linear combination always provides a solution (cases 2 and 4 when $B_1 \neq 0$) is indicated by the purple area. The boundary of the region where the linear combination solution exists is given by $\Re(\chi) = 1$ and therefore depends on the values of C, ε, and $\bar{\nu}_{eff}$. The boundary shape is shown as a function of these parameters in Fig. 6. Increasing the inertial parameter C expands the linear combination region toward larger growth rates and frequencies, keeping its boundary at low growth rates roughly constant. In contrast, increasing the radial equilibrium flow ε shrinks the linear combination region, keeping its boundary at a constant high growth rate. When the effective collisionality $\bar{\nu}_{eff}$ increases, the linear combination region shifts toward negative growth rate values.

B. Radial mode structure

The eigenfunctions corresponding to the points labeled A–J in Fig. 5 are shown in Fig. 7. The eigenfunctions tend to develop finer radial structures at higher growth rates, in particular close to the boundary of the linear combination region. In a magnetized plasma, finite Larmor radius effects will tend to dampen perturbations at scales larger than the Larmor radius.[9] As discussed in Sec. III, capturing this effect in a fluid model requires keeping the gyroviscosity tensor in the momentum equation.[10,38] In our model, the gyroviscosity is neglected due to the lack of a closed form at an arbitrary perturbation frequency, and, as

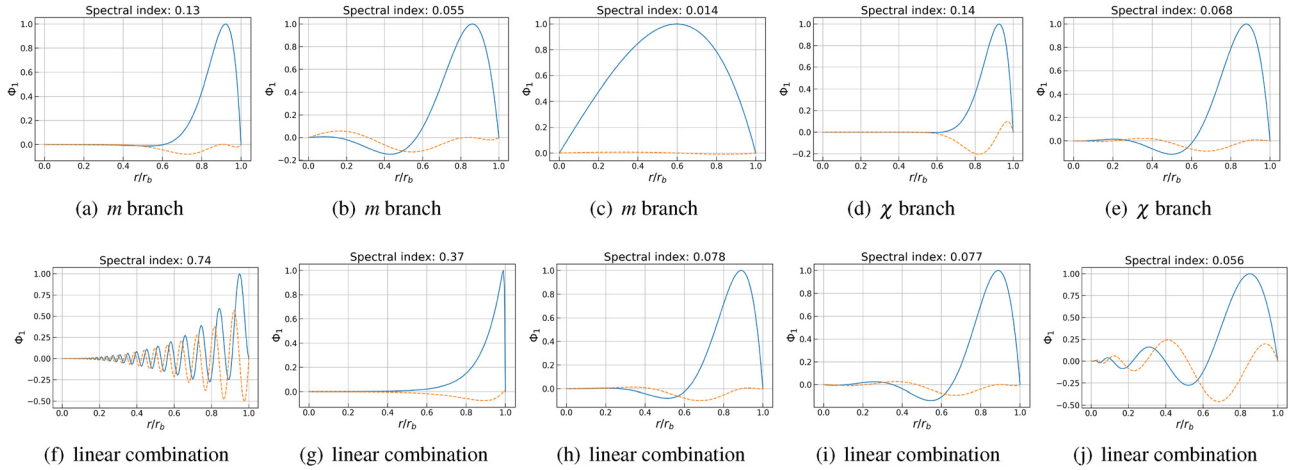

(a) m branch (b) m branch (c) m branch (d) χ branch (e) χ branch

(f) linear combination (g) linear combination (h) linear combination (i) linear combination (j) linear combination

FIG. 7. Real (blue) and imaginary (orange) parts of the eigenfunction Φ_1, as a function of the radial coordinate r normalized to the radial boundary r_b for the points labeled in Fig. 5. The k_r spectral index defined in Eq. (44) is indicated for each case.

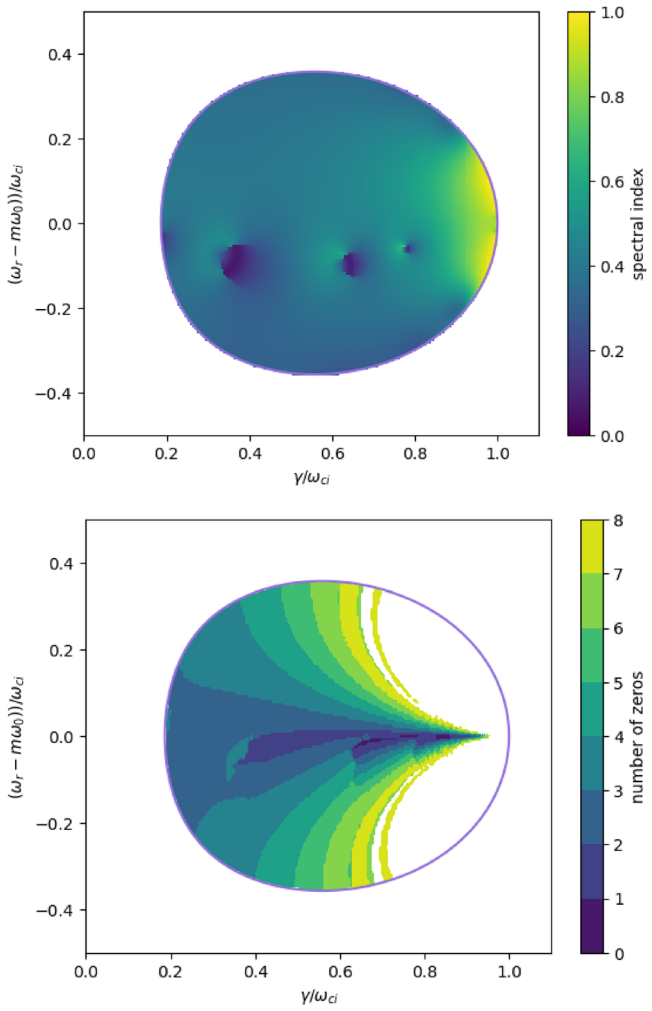

FIG. 8. Top plot: value of the spectral index $\mathscr{S}_k$ characterizing the weight of small scales in the radial structure of the eigenfunctions. Bottom plot: number of zeros for the real part of the eigenfunction Φ_1. For clarity, only values less than 8 are shown (the number of zeros rises sharply on the rightmost part of the linear combination region).

a consequence, eigenfunctions with arbitrary fine-scale structures can be obtained. The level of fine-scale structures in the radial eigenfunctions is quantified by performing the Fourier transform of Φ_1

$$\Phi_1(r) = \sum_{k_r\rho_i} \Phi_k \exp^{ik_r\rho_i\bar{r}}, \tag{43}$$

and introducing the spectral index

$$\mathscr{S}_k = \sqrt{\frac{\sum_{k_r\rho_i>1} |\Phi_k|^2}{\sum_{k_r\rho_i} |\Phi_k|^2}}. \tag{44}$$

The spectral index $\mathscr{S}_k$ quantifies the fraction of spectral components at scales smaller than the ion Larmor radius. Choosing a slightly different scale for the cutoff, e.g., $k_r\rho_i > 0.8$ or $k_r\rho_i > 1.2$ does not significantly modify the results. The value of the spectral index within the linear combination region is represented in Fig. 8 (top plot) together with the number of zeros of $\Re(\Phi_1)$ in the interval $0 < r < r_b$ (bottom plot).

Consistent with Fig. 5, high values of the spectral index (small-scale radial structures) are located on the rightmost part of the linear combination region and correspond to solutions radially oscillating, case F, or strongly localized at the plasma periphery, case G. The number of zeros, n, allows one to distinguish between these two cases. Finite Larmor radius effects can be crudely introduced in the model by setting a threshold for S_k, for instance, 10%, above which the solution is discarded. Similarly, a cutoff can be introduced in the azimuthal direction and imposed $k_\theta\rho_i < 1$, where the azimuthal wave vector $k_\theta = m/r$ can be assessed at a representative radius $r = r_0$. For typical MISTRAL plasmas, $\rho_i = 1$–$2\,\mathrm{cm}$ and $r_0 = 6$ cm, leading to $m_{max} = 3$–6.

VI. LINEAR STABILITY

A. $\delta\bar{\omega}_0$ driven instability ($\bar{\nu}_{ir_0}=0$, $\bar{\mu}=0$)

A simplified dispersion relation is examined first in the limits $\varepsilon = 0$ and $\bar{\mu} = 0$ (no radial flow, no ionization). From Eq. (36), one gets

$$\Phi_1'' + \left(\frac{1}{\bar{r}} - \frac{1}{\bar{L}_n}\right)\Phi_1' - \frac{m^2}{\bar{r}^2}\Phi_1 + \frac{1}{\bar{r}\bar{L}_n}N\Phi_1 = 0, \tag{45}$$

where

$$\frac{N}{m} = \frac{C}{\bar{\omega}_c} - \frac{C^2 - \bar{\omega}_c^2}{\bar{\omega}_{ph} + m\delta\bar{\omega}_0}\frac{\bar{\omega}_{ph}}{\bar{\omega}_c}. \tag{46}$$

The approach to solve this differential equation and obtain the values of N is the same as given in Refs. 10, 16, and 23 for the collisionless case (for which $\bar{\omega}_c = \bar{\omega}_{ph}$). Once N is known, substituting $\bar{\omega}_c = \bar{\omega}_{ph} + i\bar{\nu}_{eff}$ in Eq. (46) and rearranging it, a cubic equation in $\bar{\omega}_{ph}$ is obtained

$$\begin{aligned}\bar{\omega}_{ph}^3 &- \left(\frac{N}{m} - 2i\bar{\nu}_{eff}\right)\bar{\omega}_{ph}^2 \\ &+ \left(C - C^2 - \frac{N}{m}(m\delta\bar{\omega}_0 + i\bar{\nu}_{eff}) - \bar{\nu}_{eff}^2\right)\bar{\omega}_{ph} \\ &+ (mC - iN\bar{\nu}_{eff})\delta\bar{\omega}_0 = 0.\end{aligned} \tag{47}$$

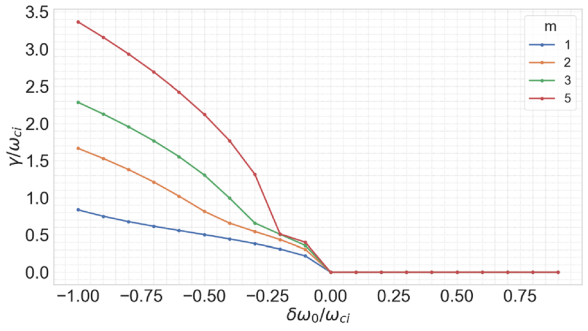

FIG. 9. Normalized growth rate γ/ω_{ci} as a function of $\delta\omega_0/\omega_{ci}$ for azimuthal mode numbers $m = 1, 2, 3$, and 5 obtained using the dispersion relation given by Eq. (48).

Let us first discuss the origin of the different terms in Eq. (47). The inertial term $(\mathbf{v}_i \cdot \nabla)\mathbf{v}_i$ and the Lorentz force present in the linearized ion momentum equation lead to the magnetization factor $C = 1 + 2\bar{\omega}_0$, where the contribution $2\bar{\omega}_0$ is due to the inertial effects. When inertial effects are neglected, $C = 1$ in Eq. (47). In addition, the inertial term introduces a Doppler shift in the perturbation frequency $\bar{\omega}_{ph} = \bar{\omega} - m\bar{\omega}_0$. The effects resulting from ion–neutral collisions and ionization frequency enter through the term $\bar{\nu}_{eff}$. Setting $C = 1$, $\bar{\omega}_{ph} = \bar{\omega}$ (no inertial effects), and $\bar{\nu}_{eff} = 0$ (no collisions), the dispersion relation given by Eq. (47) reduces to

$$\bar{\omega}^3 - \frac{N}{m}\bar{\omega}^2 - N\delta\bar{\omega}_0\bar{\omega} + m\delta\bar{\omega}_0 = 0. \tag{48}$$

The only destabilization factor present in Eq. (48) is $\delta\bar{\omega}_0 = \bar{\omega}_0 - \bar{\omega}_{E0} - \bar{\omega}_{*0}$. It represents the competition between the advection by the background ion flow (ω_0), the advection by the background electron flow (ω_{E0}), and the advection by the perturbed $\mathbf{E} \times \mathbf{B}$ flow in the background density gradient ω_{*0}, see Eqs. (18) and 19), in generating the density perturbation. Unstable modes (positive growth rate) are only obtained for $\delta\bar{\omega}_0 < 0$, i.e., $\bar{\omega}_0 < \bar{\omega}_{E0} + \bar{\omega}_{*0}$, as shown in Fig. 9 for different azimuthal mode numbers m and the radial mode number $n = 0$. It is verified that for $\delta\bar{\omega}_0 \geq 0$, no instability is obtained ($\bar{\gamma} = 0$), irrespective of the values of $\bar{\nu}_{eff}$ and C in Eq. (47).

The instability stems from the divergent particle flux driven by the electron flow and the ion azimuthal flow when $\delta\bar{\omega}_0 < 0$, i.e., when $\bar{\omega}_0 < \bar{\omega}_{E0} + \bar{\omega}_{*0}$. This condition can be met for both positive and negative radial electric fields, depending on the magnitude and direction of the density gradient. In practice, the equilibrium azimuthal flow leads to a finite value of $\delta\bar{\omega}_0$ when inertia, collisions, or both are considered, see Eq. (10).

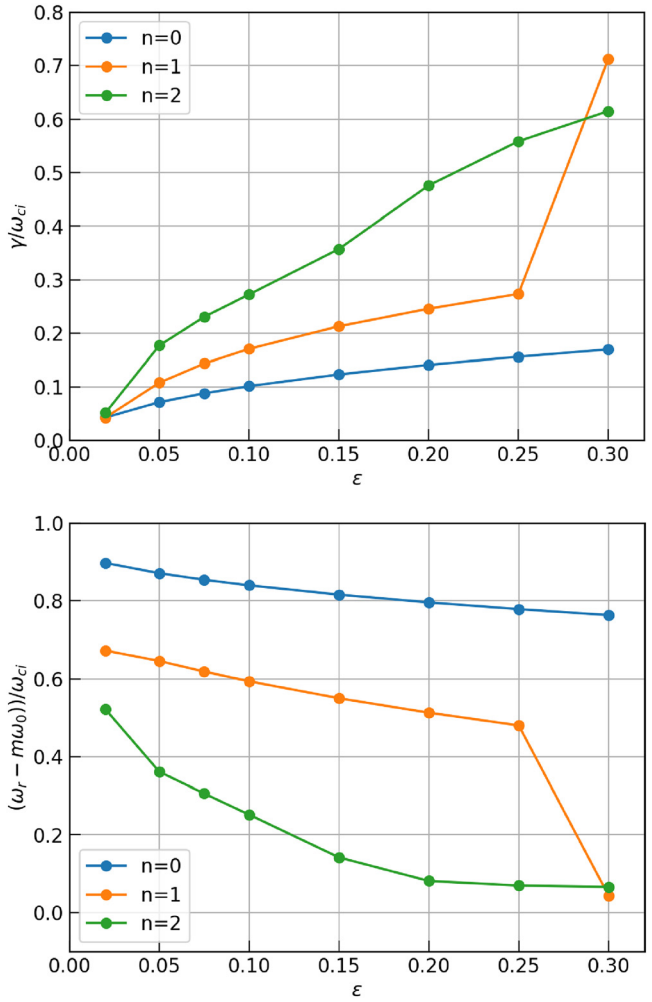

FIG. 10. Growth rate (top) and mode frequency (bottom) of the m branch, as a function of the ion equilibrium radial flow ε for $m = 1$, low spectral index $\mathscr{S}_k < 0.1$, and the number of zeros of the eigenfunction n as indicated in the legend. The inputs used in Eq. (36) are $\bar{r}_b = 5.54$, $r_0 = 10/3$, $\delta\bar{\omega}_0 = 0$, $\bar{\nu} = 0$, $\bar{\mu} = 0$, $\bar{\omega}_0 = 0.48$, and $C = 1$.

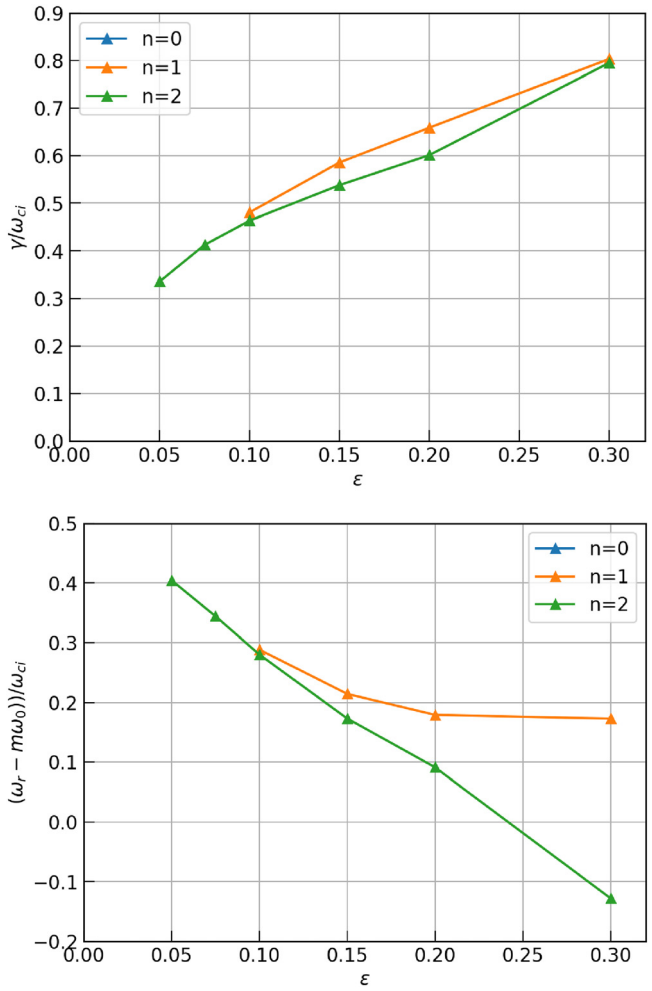

FIG. 11. Growth rate (top) and mode frequency (bottom) of the linear combination solution, as a function of the ion equilibrium radial flow ε for $m = 1$ and low spectral index $\mathscr{S}_k < 0.1$. The number of zeros of the eigenfunction n is indicated in the legend. The inputs used in Eq. (36) are $\bar{r}_b = 5.54$, $r_0 = 10/3$, $\delta\bar{\omega}_0 = 0$, $\bar{\nu} = 0$, $\bar{\mu} = 0$, $\bar{\omega}_0 = 0.48$, and $C = 1$.

B. Radial flow driven instability ($\delta\bar{\omega}_0=0$, $\bar{v}_{ir_0} \neq 0$)

1. Impact of a finite radial flow (ε)

Another driving factor for the instability is the presence of an ion equilibrium radial flow $\bar{v}_{ir_0} = -\bar{r}\varepsilon$. A radial equilibrium flow naturally arises in the presence of a central ionization source or when ion–neutral friction is included, see Eq. (8). To focus on the mechanism of the instability driven by the ion radial flow, we set $\delta\bar{\omega}_0 = 0$ in Eq. (36). In addition, we assume $\bar{\nu}_{in} = 0$, $\bar{\mu} = 0$, and $C = 1$. The impact of the radial equilibrium flow is investigated by independently varying the parameter ε. Note that with $\delta\bar{\omega}_0 = 0$ and $C = 1$, the ion azimuthal flow $\bar{\omega}_0$ only modifies the Doppler-shifted frequency $\bar{\omega}_{ph}$. The stability of the m branch is investigated in Fig. 10, focusing on solutions with a low spectral index, $\mathscr{S}_k < 0.1$, and $n \leq 2$, where n is the number of zeros of the real part of the solution Φ_1 for $0 < r < r_b$. For each value of ε, when several solutions are obtained with the same number of zeros n, only the one with the highest growth rate is shown. For all modes, the growth rate increases with the radial equilibrium flow ε, with the largest n modes having the largest growth rate. The Doppler-shifted mode frequency is large, with values comparable to the ion cyclotron frequency for $n = 0$, and decreases when ε increases, with a stronger decrease for high n modes.

In contrast to the results obtained for the m branch, low n modes are not found to be unstable for the χ branch, with all unstable modes having $n \geq 3$. The spectral index $\mathscr{S}_k$ is also larger and only gets smaller than 0.1 for $\varepsilon > 0.15$. Increasing ε leads to an increase in the growth rate of the most unstable mode and its number of zeros n. For all modes of the χ branch, the mode frequency remains close to zero, with a magnitude less than 15% of the ion cyclotron frequency. Finally, the linear combination solution is investigated, again focusing on the cases with $\mathscr{S}_k < 0.1$ and $n \leq 2$. The results are shown in Fig. 11. For each number of zeros n, only the most unstable mode is shown. No $n = 0$ modes are found to be unstable. Modes with $n = 1$–2 are destabilized by the ion radial flow, and their growth rate increases with ε. Interestingly, at low ε, the growth rate of the modes of the linear combination solution is larger than that of the m branch solution. The mode frequency is about half of the ion cyclotron frequency at low ε and decreases when ε increases. In contrast to the m branch, at a given ε, the values of the growth rate and the mode frequency do not vary much with n.

In conclusion, an instability is driven by a finite equilibrium radial ion flow. Different branches can be excited. The χ branch tends to be unstable at high n and spectral index values, while the m branch and the linear combination are found to be unstable at low values of n and $\mathscr{S}_k$. For all cases, the maximum growth rate increases with the radial flow parameter ε, and the instability disappears when $\varepsilon \to 0$.

2. Azimuthal mode number spectrum

The azimuthal mode number m dependence of the ion radial flow instability is now investigated for $\varepsilon = 0.2$. As in Sec. VI B 1, we set $\delta\bar{\omega}_0 = 0$, $\bar{\nu}_{in} = 0$, $\bar{\mu} = 0$, and $C = 1$. The χ branch exhibits high zero numbers, $n \geq 3$, and a high spectral index, $\mathscr{S}_k$, with a tendency to excite radial structures with smaller scales and higher n when m is increased. The variation in mode frequency remains quite limited. In Fig. 12, the azimuthal mode number spectra obtained for the m branch and the linear combination are shown together, focusing on the cases with $\mathscr{S}_k < 0.1$ and $n \leq 2$. The growth rate of the linear combination solution decreases rapidly at high m, without an unstable linear combination solution for $m \geq 4$. The m branch exhibits a very moderate increase in the mode growth rate with the azimuthal mode number m and a more marked increase with the number of zeros n. Similarly, the mode frequency slowly decreases with m and decreases more markedly with n. Interestingly, the linear combination solution is the most unstable at low m, resulting in a maximum growth rate at $m = 1$.

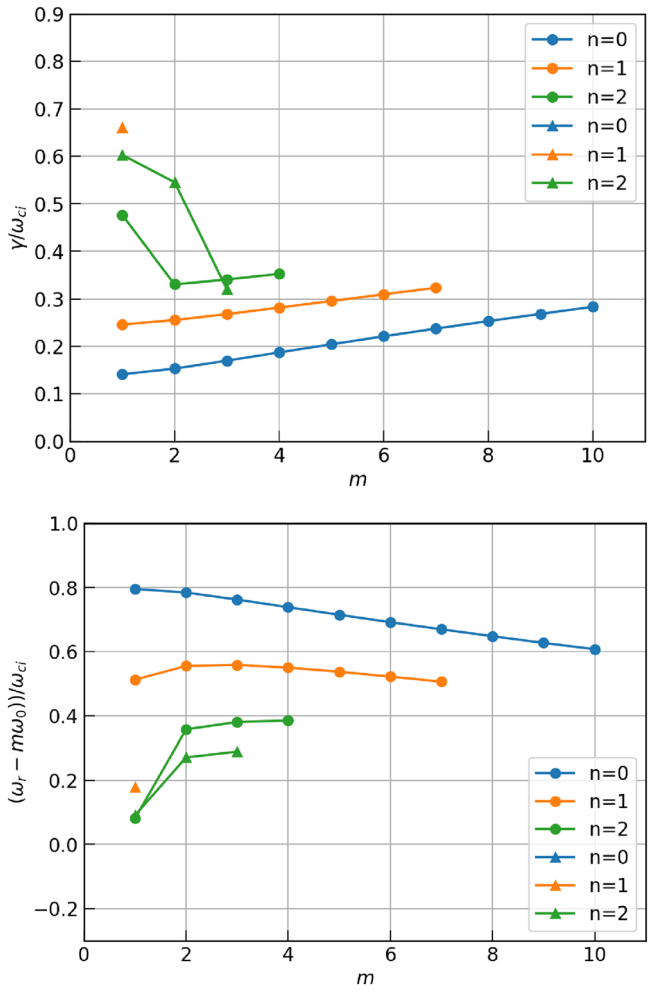

FIG. 12. Growth rate (top) and mode frequency (bottom) of the m branch (circles) and of the linear combination solution (triangles), as a function of the azimuthal mode number m for $\varepsilon = 0.2$, keeping only solutions with $\mathscr{S}_k < 0.1$. The number of zeros of the eigenfunction is indicated in the legend. The inputs used in Eq. (36) are $\bar{r}_b = 5.54$, $r_0 = 10/3$, $\delta\bar{\omega}_0 = 0$, $\bar{\nu} = 0$, $\bar{\mu} = 0$, $\bar{\omega}_0 = 0.48$, and $C = 1$.

3. Impact of collisionality and ionization

The impact of collisionality and ionization is now examined for the case explored in the Sec. VI B 2. The ion–neutral collisionality $\bar{\nu}_{in}$ and the ionization parameter $\bar{\mu}$ are varied, keeping the other inputs constant (no self-consistent variation of the ion background flow and

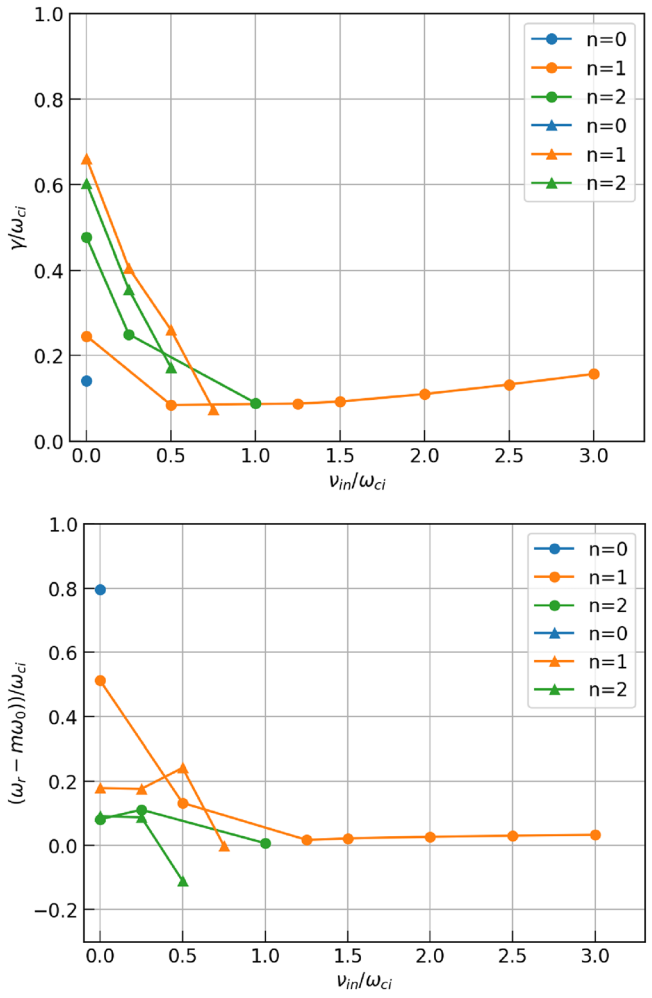

FIG. 13. Growth rate (top) and mode frequency (bottom) of the m branch (circles) and of the linear combination solution (triangles), as a function of the ion–neutral collisionality for $m = 1$ and $\varepsilon = 0.2$, keeping only solutions with $\mathscr{S}_k < 0.1$. The number of zeros of the eigenfunction is indicated in the legend. The inputs used in Eq. (36) are $\bar{r}_b = 5.54$, $r_0 = 10/3$, $\delta\bar{\omega}_0 = 0$, $\bar{\mu} = 0$, $\bar{\omega}_0 = 0.48$, and $C = 1$.

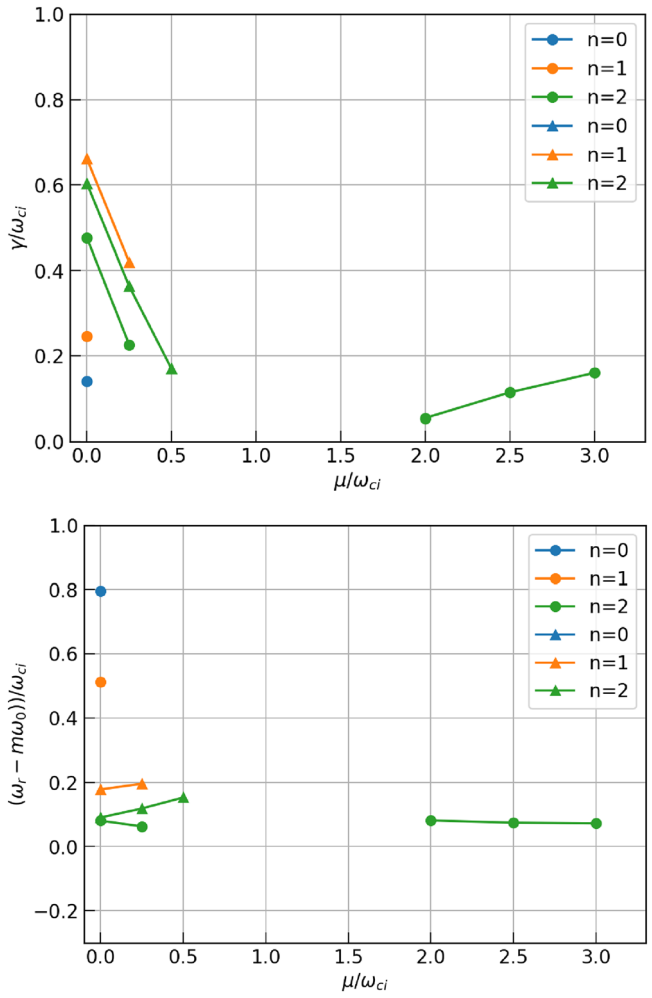

FIG. 14. Growth rate (top) and mode frequency (bottom) of the m branch (circles) and of the linear combination solution (triangles), as a function of the ionization parameter for $m = 1$ and $\varepsilon = 0.2$, keeping only solutions with $\mathscr{S}_k < 0.1$. The number of zeros of the eigenfunction is indicated in the legend. The inputs used in Eq. (36) are $\bar{r}_b = 5.54$, $r_0 = 10/3$, $\delta\bar{\omega}_0 = 0$, $\bar{\nu}_{in} = 0$, $\bar{\omega}_0 = 0.48$, and $C = 1$.

other parameters). As in Secs. VI B 1 and VI B 2, only solutions with $\mathscr{S}_k < 0.1$ and $n \leq 2$ are displayed since they are the most relevant in a weakly magnetized plasma.

The variation in mode growth rate and frequency is shown in Fig. 13 as a function of the ion–neutral collisionality $\bar{\nu}_{in}$ for the m branch and the linear combination solution. The linear combination only exists at low collisionality since the existence domain is shifted toward stable modes ($\bar{\gamma} < 0$) when $\bar{\nu}_{in}$ increases, as shown in Fig. 6. When the linear combination solution exists, the χ branch is also found to be unstable, but only with very high radial mode numbers or a low growth rate. At zero collisionality, the linear combination solution is the most unstable, which was already observed in Fig. 12 for $m = 1$. When collisionality increases, both the m branch and the linear combination solution are strongly stabilized, and the real frequency of

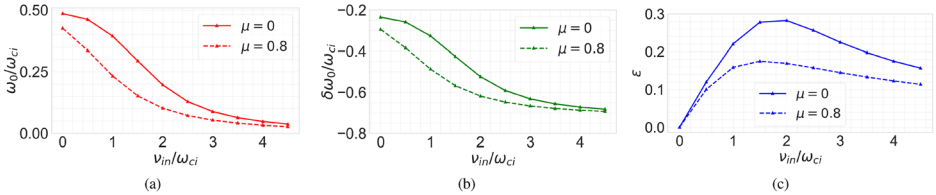

FIG. 15. Variation of (a) $\bar{\omega}_0$, (b) $\delta\bar{\omega}_0$, and (c) ε, as a function of normalized ion–neutral collision frequency ν_{in}/ω_{ci} for two different values of $\bar{\mu} = 0$ (solid lines) and $\bar{\mu} = 0.8$ (dashed lines) with $\bar{\omega}_{E0} = 0.9$ and $\bar{\omega}_{*0} = -0.18$.

the m branch decreases. Then, as collisionality increases further, the m branch develops an instability with a low growth rate, which increases slowly with $\bar{\nu}_{in}$, and a Doppler shifted frequency close to zero.

The impact of the ionization parameter $\bar{\mu}$ is examined in Fig. 14. Collisionality and ionization have the same impact on the frequency $\bar{\omega}_c$ for which the dispersion relation is solved, since $\bar{\omega}_c = \bar{\omega} - m\bar{\omega}_0 + i\bar{\nu}_{eff}$ with $\bar{\nu}_{eff} = \bar{\nu}_{in} + \bar{\mu}$. Increasing ionization, therefore, leads to a shift of the existence domain of the linear combination branch toward stable modes in the same way as increasing collisionality does. However, there is an additional effect of increasing the ionization parameter induced by the terms proportional to $\bar{\mu}$ in the dispersion relation Eq. (36). Nevertheless, Fig. 14 shows that qualitatively the increase in $\bar{\mu}$ has the same effect as the increase in $\bar{\nu}_{in}$. It first leads to a strong stabilization of the linear combination solution and of the m branch. The m branch then develops a solution with low frequency and a growth rate, increasing with $\bar{\mu}$. At intermediate $\bar{\mu}$ values, no solution with low radial spectral content ($\mathscr{S}_k < 0.1$ and $n \leq 3$) is obtained. This is in contrast with the effect of collisionality, for which this intermediate region without low radial spectral content instability does not develop.

In addition to their direct impact on the dispersion relation, collisionality and ionization modify the ion background flow, see Eq. (10), which will also affect linear stability. As an illustration, the variation of ε, $\bar{\omega}_0$, and $\delta\bar{\omega}_0$ is shown in Fig. 15 for a scan in $\bar{\nu}_{in}$ at two different values of $\bar{\mu}$. Increasing collisionality (or ionization), damps the ion azimuthal flow $\bar{\omega}_0$ toward zero. As a consequence, the drive for the centrifugal instability first becomes stronger ($\delta\bar{\omega}_0$ becomes more negative) and then saturates. Regarding the drive for the ion radial flow instability, ε first increases almost linearly with increasing collisionality, and then saturates and decreases slowly as $\bar{\omega}_0$ approaches zero.

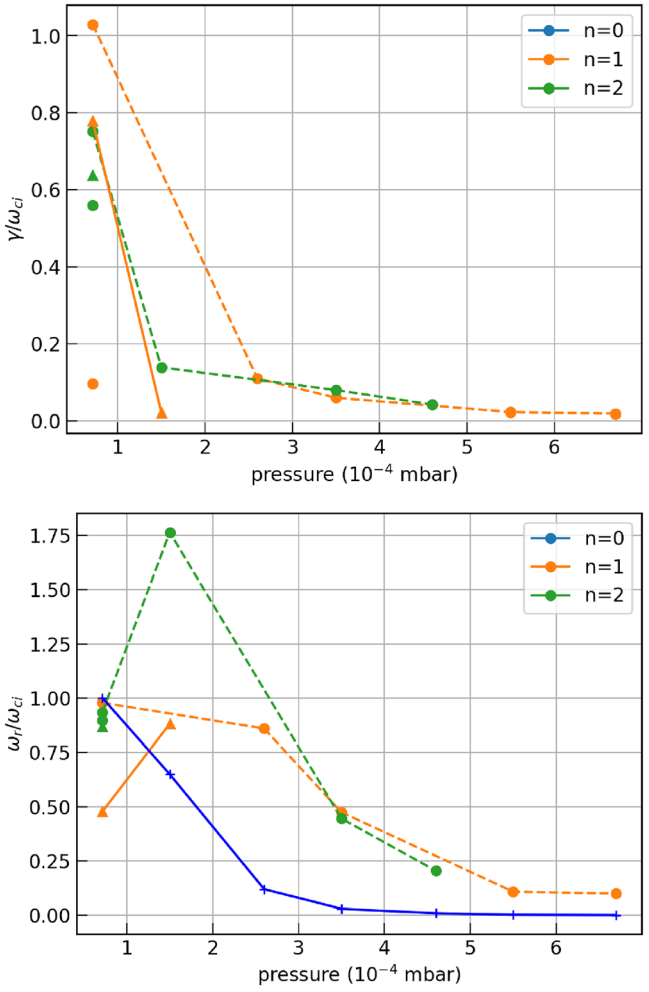

FIG. 16. Growth rate (top) and mode frequency (bottom) of the m branch (circles) and of the linear combination solution (triangles) for the $m = 1$ mode with $\mathscr{S}_k < 0.1$ (full lines) and $0.1 < \mathscr{S}_k < 0.2$ (dashed lines), as a function of the neutral pressure for the input parameters listed in Table II (MISTRAL plasma at $B = 160$ G). The number of zeros of the eigenfunction n is indicated in the legend. The computed ion azimuthal flow $\bar{\omega}_0$ is shown with the blue line.

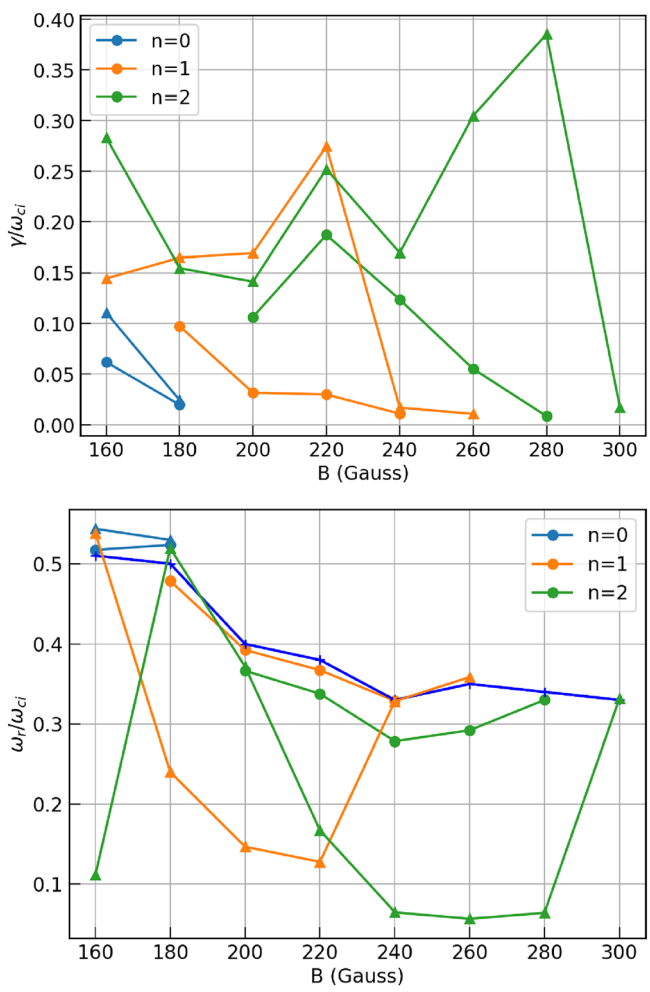

FIG. 17. Growth rate (top) and mode frequency (bottom) of the m branch (circles) and of the linear combination solution (triangles) for the $m = 1$ mode with a low spectral index, $\mathscr{S}_k < 0.1$, as a function of the magnetic field for the input parameters listed in Table III (MISTRAL plasma at $P = 1.04 \times 10^{-4}$ mbar). The number of zeros of the eigenfunction n is indicated in the legend. The computed ion azimuthal flow $\bar{\omega}_0$ is shown with the blue line.

C. Linear stability of MISTRAL plasmas

We now investigate the linear stability of MISTRAL plasmas for the scans in neutral pressure and magnetic field described in Appendix A and Fig. 4. The inputs used to solve Eq. (36) are listed in Tables II and III.

The results obtained for the pressure scan (see Fig. 16) follow the general trend obtained for the collisionality and ionization scans that were performed in Sec. VI B 3, without considering the self-consistent evolution of the electric field and background ion azimuthal flow. That is, the linear combination solution provides the most unstable modes with low zero numbers n and low radial spectral content $\mathscr{S}_k < 0.1$, at low pressure. Then comes the solution of the m branch. Their Doppler-shifted frequency is negative (linear combination) or close to zero (m branch), leading to a real frequency less than (linear combination) or close to (m branch) ω_0. When pressure is increased, the m branch and linear combination modes are strongly stabilized. The linear combination region quickly vanishes, and the remaining unstable modes are obtained from the m branch at higher spectral content $0.1 < \mathscr{S}_k < 0.2$. These modes have a low growth rate and a positive Doppler-shifted frequency that gets smaller as the pressure further increases. The χ branch only provides modes with high spectral content or very low growth rates, as previously observed.

We then focus on the linear stability of MISTRAL plasmas in a magnetic field scan performed at low pressure ($P = 1.04 \times 10^{-4}$ mbar). The mode growth rate and the real frequency are shown in Fig. 17 for modes with a low number of zeros n and low radial spectral content. At all values of the magnetic field, the linear combination solution leads to the largest growth rate for low spectral index modes, then comes the m branch and finally the χ branch (not shown). In contrast to the pressure scan, the linear combination region exists across the whole magnetic field scan, with higher growth rates obtained at a higher magnetic field. For the linear combination solution and the χ branch, $n = 0$ and $n = 1$ modes are only obtained at low magnetic fields. The Doppler-shifted frequency is close to zero for the m branch and negative for the linear combination solution.

Figures 16 and 17 show that instabilities driven by the ion radial flow are predicted to be the most unstable in low-pressure MISTRAL plasmas, and that accounting for this drive in a linear stability study is necessary.

VII. SUMMARY

A two-fluid theory to study the instabilities in weakly magnetized plasmas with an $\mathbf{E} \times \mathbf{B}$ configuration prone to the formation of rotating spokes is presented in this paper. The model is radially global and is not limited to frequencies much smaller than the ion cyclotron frequency. It extends the previous work[23] to include the impact of ion–neutral collisionality, the ionization source, and, most importantly, the background radial ion flow. Ion finite Larmor radius (FLR) effects are considered by introducing an *ad hoc* cutoff at small scales. The derived third-order differential equation, Eq. (36), is solved numerically as an eigenvalue problem to determine the growth rate, the real part of the perturbation frequency, and the associated radial eigenmodes for a given azimuthal mode number m. The well-known centrifugal instability, driven by the differential azimuthal rotation of ions and electrons, is recovered by the model. The main finding of the paper is that the background radial ion flow also drives an instability whose growth rate increases with the flow amplitude. This instability has two main branches labeled the m branch and the χ branch, plus their linear combination. The most relevant solutions in a weakly magnetized plasma are the m branch and the linear combination, since the χ branch exhibits small-scale radial structures that would be damped by the ion FLR effects. Interestingly, the linear combination has an azimuthal mode spectrum that peaks at $m = 1$. The m branch has a more standard behavior, with a growth rate that slowly increases with m. Both the ion–neutral collisions and the ionization frequency strongly stabilize the linear combination solution and the m branch. At high collisionality or ionization frequency, only the m branch survives, with a small growth rate and a Doppler-shifted frequency close to zero. Application of the linear stability model to MISTRAL plasmas reveals that the background ion radial flow plays a key role in determining the most unstable mode, in particular at low pressure. How these linear instabilities saturate in the non-linear regime will be the object of future work, to allow for direct comparisons with MISTRAL plasmas.

ACKNOWLEDGMENTS

The authors are very grateful to Olivier Agullo for his recommendations to solve the third-order differential equation obtained from the model. This research was funded, in whole or in part, by l'Agence Nationale de la Recherche (ANR), project CANTALOUPE ANR-24-CE30-0324.

AUTHOR DECLARATIONS

Conflict of Interest

The authors have no conflicts to disclose.

Author Contributions

S. Aggarwal: Conceptualization (equal); Data curation (equal); Formal analysis (equal); Investigation (equal); Methodology (equal); Validation (equal); Visualization (equal); Writing – original draft (equal); Writing – review & editing (equal). **Y. Camenen:** Conceptualization (equal); Data curation (equal); Formal analysis (equal); Investigation (equal); Methodology (equal); Supervision (equal); Validation (equal); Visualization (equal); Writing – original draft (equal); Writing – review & editing (equal). **A. Escarguel:** Conceptualization (equal); Data curation (equal); Formal analysis (equal); Investigation (equal); Methodology (equal); Supervision (equal); Validation (equal); Visualization (equal); Writing – original draft (equal); Writing – review & editing (equal). **A. Poyé:** Conceptualization (equal); Data curation (equal); Formal analysis (equal); Investigation (equal); Methodology (equal); Supervision (equal); Validation (equal); Visualization (equal); Writing – original draft (equal); Writing – review & editing (equal).

DATA AVAILABILITY

The data that support the findings of this study are available from the corresponding author upon reasonable request.

APPENDIX A: INTERMEDIATE STEPS IN THE DISPERSION RELATION DERIVATION

The various contributions in Eq. (34) are

$$
\begin{aligned}
n_0\nabla\cdot\bar{\mathbf{v}}_{i1}^{(0)} &= n_0\frac{C}{C^2-\bar{\omega}_c^2}\left[\frac{i\bar{\omega}_c}{C}\nabla^2\Phi_1\right.\\
&\quad\left.+\lambda\bar{\mu}\bar{\omega}_0\left(\frac{m\bar{\omega}_c}{C}\Phi_1+2\Phi_1+\bar{r}\Phi_1'\right)\right],\\
\bar{\mathbf{v}}_{i1}^{(0)}\cdot\nabla n_0 &= \frac{C}{C^2-\bar{\omega}_c^2}\left[-\frac{im}{\bar{r}}\Phi_1 n_0'+\frac{i\bar{\omega}_c}{C}\Phi_1' n_0'+\lambda\bar{\mu}\bar{r}\bar{\omega}_0\Phi_1 n_0'\right],\\
n_0\nabla\cdot\bar{\mathbf{v}}_{i1}^{(1)} &= n_0\frac{C^2+\bar{\omega}_c^2}{(C^2-\bar{\omega}_c^2)^2}\left[\bar{r}\Phi_1'''+3\Phi_1''-\frac{m^2}{\bar{r}}\Phi_1'+\frac{1}{\bar{r}}\Phi_1'\right]\\
&\quad-n_0\lambda\bar{\mu}\frac{C^2+\bar{\omega}_c^2}{(C^2-\bar{\omega}_c^2)^2}[im\bar{\omega}_0(2\Phi_1+\bar{r}\Phi_1')\\
&\quad+\frac{2iC\bar{\omega}_c}{C^2+\bar{\omega}_c^2}(4\Phi_1+5\bar{r}\Phi_1'+\bar{r}^2\Phi_1'')\bar{\omega}_0\\
&\quad-\left(\frac{C^2-\bar{\omega}_c^2}{C^2+\bar{\omega}_c^2}\right)\left(i\bar{\omega}_c(2\Phi_1+\bar{r}\Phi_1')+imC\Phi_1\right)\Bigg],\\
\bar{\mathbf{v}}_{i1}^{(1)}\cdot\nabla n_0 &= n_0\frac{C^2+\bar{\omega}_c^2}{(C^2-\bar{\omega}_c^2)^2}\left(-\frac{\bar{r}\Phi_1''}{\bar{L}_n}-\frac{\Phi_1'}{\bar{L}_n}+\frac{2mC\bar{\omega}_c}{C^2+\bar{\omega}_c^2}\frac{\Phi_1'}{\bar{L}_n}\right)\\
&\quad-n_0\lambda\bar{\mu}\frac{C^2+\bar{\omega}_c^2}{(C^2-\bar{\omega}_c^2)^2}\left[-\frac{2iC\bar{\omega}_c}{C^2+\bar{\omega}_c^2}(2\Phi_1+\bar{r}\Phi_1')\frac{\bar{r}\bar{\omega}_0}{\bar{L}_n}\right.\\
&\quad\left.+\left(\frac{C^2-\bar{\omega}_c^2}{C^2+\bar{\omega}_c^2}\right)\frac{i\bar{\omega}_c\bar{r}}{\bar{L}_n}\Phi_1\right],\\
n_1\nabla\cdot\bar{\mathbf{v}}_{i0} &= -2\varepsilon n_1,\\
\bar{\mathbf{v}}_{i0}\cdot\nabla n_1 &= im\bar{\omega}_0 n_1-\bar{r}\varepsilon n_1',
\end{aligned}
\tag{A1}
$$

where $\nabla^2\Phi_1=\Phi_1''+\Phi_1'/r-(m^2/r^2)\Phi_1$.

Substituting the required values in Eq. (34) and then implementing the condition of quasi-neutrality given by Eq. (35), we get

$$
\begin{aligned}
&\frac{im}{\bar{r}}\frac{1}{\bar{L}_n}\tau\bar{\phi}_1+im\bar{\omega}_{E0}\bar{n}_1\\
&=\frac{i\bar{\omega}_c}{C^2-\bar{\omega}_c^2}\left[\Phi_1''+\left(\frac{1}{\bar{r}}-\frac{1}{\bar{L}_n}\right)\Phi_1'-\frac{m^2}{\bar{r}^2}\Phi_1\right.\\
&\quad\left.+\frac{m}{\bar{r}\bar{L}_n}\frac{C}{\bar{\omega}_c}\Phi_1\right]+\varepsilon\frac{C^2+\bar{\omega}_c^2}{(C^2-\bar{\omega}_c^2)^2}\left[\bar{r}\Phi_1'''+\left(3-\frac{\bar{r}}{\bar{L}_n}\right)\Phi_1''\right.\\
&\quad\left.-\left(\frac{m^2-1}{\bar{r}}+\frac{1}{\bar{L}_n}\right)\Phi_1'+\frac{2mC\bar{\omega}_c}{\bar{L}_n(C^2+\bar{\omega}_c^2)}\Phi_1'\right]\\
&\quad+\lambda\bar{\mu}\left(\frac{C}{C^2-\bar{\omega}_c^2}\right)\left[\left(\frac{m\bar{\omega}_c}{C}-\frac{\bar{r}}{\bar{L}_n}+2\right)\bar{\omega}_0\Phi_1+\bar{r}\bar{\omega}_0\Phi_1'\right]\\
&\quad-\varepsilon\lambda\bar{\mu}\frac{C^2+\bar{\omega}_c^2}{(C^2-\bar{\omega}_c^2)^2}\left[\frac{2iC\bar{\omega}_c}{C^2+\bar{\omega}_c^2}\bar{r}\bar{\omega}_0(\bar{r}\Phi_1''\right.\\
&\quad+\bar{r}\left(\frac{5}{\bar{r}}-\frac{1}{\bar{L}_n}\right)\Phi_1'+2\left(\frac{2}{\bar{r}}-\frac{1}{\bar{L}_n}\right)\Phi_1)+im\bar{\omega}_0(2\Phi_1+\bar{r}\Phi_1')\\
&\quad\left.-\frac{C^2-\bar{\omega}_c^2}{C^2+\bar{\omega}_c^2}\left(i\bar{r}\bar{\omega}_c\Phi_1'+imC\Phi_1+i\bar{r}\bar{\omega}_c\left(\frac{2}{\bar{r}}-\frac{1}{\bar{L}_n}\right)\Phi_1\right)\right]\\
&\quad-2\varepsilon\bar{n}_1+im\bar{\omega}_0\bar{n}_1-\bar{r}\varepsilon\frac{n_1'}{n_0}.
\end{aligned}
\tag{A2}
$$

Using the electron continuity equation, Eq. (19), and the relation, $\Phi_1=\bar{n}_1+\tau\bar{\phi}_1$, we can write

$$
\Phi_1=(1+\alpha_*)\tau\bar{\phi}_1. \tag{A3}
$$

Furthermore, n_1'/n_0 can be expressed as a function of Φ_1 using Eq. (19) and employing the relation $\Phi_1=\bar{n}_1+\tau\bar{\phi}_1$

$$
n_1'=-\frac{m\bar{\omega}_{*0}}{\bar{\omega}_{ph}+m\delta\bar{\omega}_0}\left(n_0'\Phi_1+n_0\Phi_1'\right), \tag{A4}
$$

which, when divided by n_0 becomes

$$
\frac{n_1'}{n_0}=\frac{m\bar{\omega}_{*0}}{\bar{\omega}_{ph}+m\delta\bar{\omega}_0}\left(\frac{\Phi_1}{\bar{L}_n}-\Phi_1'\right). \tag{A5}
$$

Eliminating $\bar{n}_1$, $\tau\bar{\phi}_1$, and n_1'/n_0 from Eq. (A2), a third-order linear homogeneous differential equation in Φ_1 is obtained, which is given by Eq. (36).

APPENDIX B: EXPERIMENTAL CHARACTERIZATION OF MISTRAL PLASMAS

1. Variation of MISTRAL characteristic frequencies in a pressure scan and a magnetic field scan

Experimental measurements of characteristic MISTRAL plasma parameters are presented here across a neutral pressure scan and a magnetic field scan. The density and potential profiles are measured with a radially movable Langmuir probe and are time-averaged. The parameterization of the radial profiles of number density and plasma potential is performed using Eq. (1). Then, the parameterization constants p_1, p_2, and r_0 are used to estimate $\mathbf{E}\times\mathbf{B}$ flow frequency ($\bar{\omega}_{E0}$) and diamagnetic flow frequency ($\bar{\omega}_{*0}$) using Eqs. (11) and (12), respectively. To evaluate the ion–neutral collision frequency (ν_{in}), neutral density (n_n) for a given pressure is evaluated using the relation $P=n_n k_B T_n$, where P is the neutral base pressure in Pascal, k_B is the Boltzmann constant, and T_n is the temperature of neutrals in Kelvin, assumed to be the room temperature ($T_n=300$ K). Once the neutral density is known, the momentum transfer cross section for ion–neutral collisions (σ_{in}) given by Eq. (2) in Ref. 39 is employed, and using the relation $\nu_{in}=n_n\langle\sigma_{in}v_i\rangle_v$, ν_{in} is calculated, $\langle.\rangle_v$ is the velocity average of the bracketed quantity over a Maxwellian distribution with the temperature $T_i=0.2$ eV. The calculation of $\bar{\mu}$ is described in Sec. II of Appendix B. Finally $\bar{\omega}_0$ is calculated using Eq. (7).

The evolution of these parameters in a pressure scan at a constant magnetic field $B=160$ G is given in Table II and illustrated in Fig. 4(a). The corresponding values of ω_{ci} and ρ_i are 6.1 kHz and 1.8 cm, respectively.

Similarly, Table III and Fig. 4(b) display the characteristic frequencies at different magnetic field intensities, keeping P constant at 1.04×10^{-4} mbar. Due to the variation in B, ω_{ci} and ρ_i also vary. As the ion temperature T_i is assumed to be constant, ν_{in} depends only on pressure (since the number density of neutrals changes with the change in pressure) and is constant,

$\nu_{in} = 3.76$ kHz. However, the normalized value will change due to the change in ω_{ci}.

2. Calculation of ionization frequency and the parameter $\bar{\mu}$

To calculate $\bar{\mu} = \bar{\nu}_{ion}\bar{n}_{ep}$, the fraction of primary electrons from the filaments $\bar{n}_{ep} = n_{ep}/n_0$ is assumed to be 3% based on previous experimental observations. It is important to note that the ratio n_{ep}/n_0 is plasma-dependent, and the value of 3% is only an estimate. To calculate the ionization frequency, the following approach has been used. In MISTRAL plasmas, primary electrons enter the plasma column from the source with a density n_{p1} and collide with neutral gas atoms. Some of these collisions are energetic enough to ionize the atoms, at a rate given by the ionization frequency ν_{ion1}.

After the first collision, the incoming primary electrons lost energy (15.7 eV for ionization of Ar atoms). These less energetic electrons have a density denoted by n_{p2}. Given that the energy of the primary electrons entering the source, E_b, is typically 40 eV, they can still ionize Ar atoms, at a rate represented by ν_{ion2}. After this second ionization event, the primary electrons no longer have a high enough energy to ionize Ar atoms; they will eventually thermalize after collisions. The total primary electron density can then be written as $n_{ep} = n_{p1} + n_{p2}$ and $n_{ep}/n_0 = 3\%$, leading to

$$\frac{n_{p1} + n_{p2}}{n_0} = 0.03. \tag{B1}$$

In addition,

$$\frac{\partial n_{p_2}}{\partial t} = \nu_{ion1}; (E_b) n_{p1} - \nu_{ion2}(E_b - 15.7 \quad \text{eV}) n_{p2} = 0. \tag{B2}$$

This equation simply states that, in a stationary state, the rate of production of "low energy" primary electrons, of density n_{p2}, is equal to the rate of loss of these electrons by an additional ionization event. Here, E_b is the energy of the primary electrons in eV, $E_b - 15.7$ eV represents the energy of the electrons after the first ionization. ν_{ion1} and ν_{ion2} are calculated using the formula $\nu_{ion} = n_n \sigma_{ion} v_e$, where σ_{ion}, is the electron ionization cross section given in Sec. 3.1 (Page no. 629) of Ref. 40 and v_e is the average electron velocity at the required temperature T_e ($T_e \sim 40$ eV to calculate ν_{ion1} and $T_e \sim 24.2$ eV to calculate ν_{ion2}). Once ν_{ion1} and ν_{ion2} are known, n_{p1}/n_0 and n_{p2}/n_0 can be calculated by solving Eqs. (B1) and (B2). Finally, the calculated values are used in the expression $\bar{\mu} = \bar{\nu}_{ion} n_{ep}/n_0 = (\bar{\nu}_{ion1} n_{p1} + \bar{\nu}_{ion2} n_{p2})/n_0$ to calculate $\bar{\mu}$.

APPENDIX C: SOLUTION OF EQ. (36)

We first rewrite Eq. (36) by grouping terms with respect to the power of $\bar{r}$

$$\varepsilon\Phi_1''' + \left(\frac{\mathscr{A}}{\bar{r}} + \mathscr{B}\bar{r}\right)\Phi_1'' + \left(\frac{\mathscr{C}}{\bar{r}^2} + \mathscr{D} + \mathscr{H}\bar{r}^2\right)\Phi_1' + \left(\frac{\mathscr{E}}{\bar{r}^3} + \frac{\mathscr{F}}{\bar{r}} + \mathscr{G}\bar{r}\right)\Phi_1 = 0, \tag{C1}$$

where

$$\begin{aligned}
\mathscr{A} &= 3\varepsilon + C_{NC},\\
\mathscr{B} &= \varepsilon\bar{\omega}_{*0} - i\bar{\omega}_0 a\lambda\bar{\mu}\varepsilon,\\
\mathscr{C} &= C_{NC} - \varepsilon(m^2+1),\\
\mathscr{D} &= \bar{\omega}_{*0}(C_{NC} + \varepsilon(1-am)) - \varepsilon b\lambda\\
&\quad + \frac{\lambda\bar{\mu}bC\bar{\omega}_0}{C^2 - \bar{\omega}_c^2} - \lambda\bar{\mu}\varepsilon(im\bar{\omega}_0 + 5i\bar{\omega}_0 a - C_{NC}),\\
\mathscr{E} &= -m^2 C_{NC},\\
\mathscr{F} &= -C_{NC}\bar{\omega}_{*0}N - 2\varepsilon\lambda b + \frac{\lambda\bar{\mu}bC\bar{\omega}_0}{C^2 - \bar{\omega}_c^2}\left(\frac{m\bar{\omega}_{*0}}{C} + 2\right)\\
&\quad - \lambda\bar{\mu}\varepsilon\left(2im\bar{\omega}_0 + 4i\bar{\omega}_0 a - \frac{imCb}{C^2 - \bar{\omega}_c^2} - 2C_{NC}\right),\\
\mathscr{G} &= -\varepsilon\lambda b\bar{\omega}_{*0} + \frac{\lambda\bar{\mu}bC\bar{\omega}_0}{C^2 - \bar{\omega}_c^2}\bar{\omega}_{*0} - \lambda\bar{\mu}\varepsilon\bar{\omega}_{*0}(2i\bar{\omega}_0 a - C_{NC}),\\
\mathscr{H} &= -i\bar{\omega}_0 a\lambda\bar{\mu}\varepsilon\bar{\omega}_{*0}.
\end{aligned}$$

The third-order differential equation in Φ_1 is then solved using the Cauchy–Euler formalism[41] by assuming a polynomial form for Φ_1

$$\Phi_1 = \sum_{n=0}^{\infty} a_n \bar{r}^{n+\alpha}, \tag{C2}$$

where a_n is the n^{th} term of the sum and α is not specified at this stage. The first three derivatives are

$$\begin{aligned}
\Phi_1' &= \sum_{n=0}^{\infty}(n+\alpha)a_n\bar{r}^{n+\alpha-1},\\
\Phi_1'' &= \sum_{n=0}^{\infty}(n+\alpha)(n+\alpha-1)a_n\bar{r}^{n+\alpha-2},\\
\Phi_1''' &= \sum_{n=0}^{\infty}(n+\alpha)(n+\alpha-1)(n+\alpha-2)a_n\bar{r}^{n+\alpha-3}.
\end{aligned}$$

Inserting these expressions into Eq. (C1) leads to

$$\begin{aligned}
&\varepsilon\sum_{n=0}^{\infty}(n+\alpha)(n+\alpha-1)(n+\alpha-2)a_n\bar{r}^{n+\alpha-3}\\
&\times\left(\frac{\mathscr{A}}{\bar{r}} + \mathscr{B}\bar{r}\right)\sum_{n=0}^{\infty}(n+\alpha)(n+\alpha-1)a_n\bar{r}^{n+\alpha-2}\\
&\times\left(\frac{\mathscr{C}}{\bar{r}^2} + \mathscr{D} + \mathscr{H}\bar{r}^2\right)\sum_{n=0}^{\infty}(n+\alpha)a_n\bar{r}^{n+\alpha-1}\\
&\times\left(\frac{\mathscr{E}}{\bar{r}^3} + \frac{\mathscr{F}}{\bar{r}} + \mathscr{G}\bar{r}\right)\sum_{n=0}^{\infty}a_n\bar{r}^{n+\alpha} = 0.
\end{aligned} \tag{C3}$$

Equation (C3) is a sum of polynomials equal to zero. In this equation, the coefficients of each power of $\bar{r}$ are therefore equal to zero. The indical or auxiliary equation is obtained from the coefficients of the lowest power of $\bar{r}$, i.e., from the coefficients of $\bar{r}^{\alpha-3}$

$$[\varepsilon\alpha(\alpha-1)(\alpha-2) + \mathscr{A}\alpha(\alpha-1) + \mathscr{C}\alpha + \mathscr{E}]a_0 = 0.$$

Choosing $a_0 \neq 0$, this characteristic equation has three roots: $\alpha = m, -m$ and $-C_{NC}/\varepsilon$.

The next lowest power of $\bar{r}$, i.e., $\bar{r}^{\alpha-2}$ imposes to choose $a_1 = 0$ (since m, $-m$, and $-C_{NC}/\varepsilon$ are not root of this equation). On a similar basis, it can be verified that $a_3 = a_5 = a_7 = \cdots = 0$.

Now, equating the coefficient of $\bar{r}^{\alpha-1}$ to zero in Eq. (C3), we obtain

$$a_2 = \frac{-(\mathscr{B}\alpha(\alpha-1) + \mathscr{D}\alpha + \mathscr{F})a_0}{\varepsilon\alpha(\alpha+1)(\alpha+2) + \mathscr{A}(\alpha+1)(\alpha+2) + \mathscr{C}(\alpha+2) + \mathscr{E}}, \quad \text{(C4)}$$

and similarly, equating the coefficient of $\bar{r}^{\alpha+1}$ to zero

$$a_4 = \frac{-(\mathscr{G} + \mathscr{H}\alpha)a_0 - (\mathscr{B}(\alpha+2)(\alpha-1) + \mathscr{D}(\alpha+2) + \mathscr{F})a_2}{\varepsilon(\alpha+4)(\alpha+3)(\alpha+2) + \mathscr{A}(\alpha+4)(\alpha+3) + \mathscr{C}(\alpha+4) + \mathscr{E}}. \quad \text{(C5)}$$

By recurrence, we obtain for $n \geq 4$

$$a_n = \frac{-(\mathscr{G} + \mathscr{H}(\alpha+n-4)a_{n-4} - (\mathscr{B}(\alpha+n-2)(\alpha+n-3) + \mathscr{D}(\alpha+n-2) + \mathscr{F})a_{n-2}}{\varepsilon(\alpha+n)(\alpha+n-1)(\alpha+n-2) + \mathscr{A}(\alpha+n)(\alpha+n-1) + \mathscr{C}(\alpha+n) + \mathscr{E}}. \quad \text{(C6)}$$

The final solution is the linear combination of the three independent solutions obtained from the three distinct roots, $\alpha = m$, $-m$ and $-C_{NC}/\varepsilon$

$$\Phi_1 = A_1\bar{r}^{-m}\sum_{n=0}^{\infty} a_{-m,n}\bar{r}^n + B_1\bar{r}^m\sum_{n=0}^{\infty} a_{m,n}\bar{r}^n + C_1\bar{r}^{\chi}\sum_{n=0}^{\infty} a_{\chi,n}\bar{r}^n, \quad \text{(C7)}$$

where A_1, B_1, and C_1 are integration constants, $\chi = -C_{NC}/\varepsilon$ and $a_{\alpha,n}$ is the n^{th} term of the sum with the specified α given by the recurrence relation in Eq. (C6).

For all m values where m is a positive integer, the branch $\alpha = -m$ diverges at $\bar{r} = 0$. To satisfy the boundary condition $\Phi_1(\bar{r} = 0) = 0$, we therefore choose $A_1 = 0$, leading to

$$\Phi_1 = B_1\bar{r}^m\phi_B + C_1\bar{r}^{\chi}\phi_{\chi}, \quad \text{(C8)}$$

where $\phi_B = \sum_{n=0}^{\infty} a_{m,n}\bar{r}^n$ and $\phi_{\chi} = \sum_{n=0}^{\infty} a_{\chi,n}\bar{r}^n$.

The numerical implementation of this solution in Python is open source and available at https://gitlab.com/soplasma/soplalin.

REFERENCES

[1]J. P. Boeuf and L. Garrigues, "Low frequency oscillations in a stationary plasma thruster," J. Appl. Phys. **84**, 3541–3554 (1998).
[2]S. Mazouffre, L. Grimaud, S. Tsikata, K. Matyash, and R. Schneider, "Rotating spoke instabilities in a wall-less hall thruster: Experiments," Plasma Sources Sci. Technol. **28**, 054002 (2019).
[3]T. Lafleur, S. D. Baalrud, and P. Chabert, "Theory for the anomalous electron transport in Hall effect thrusters. I. Insights from particle-in-cell simulations," Phys. Plasmas **23**, 053502 (2016).
[4]S. Xu, K. N. Ostrikov, Y. Li, E. L. Tsakadze, and I. R. Jones, "Low-frequency, high-density, inductively coupled plasma sources: Operation and applications," Phys. Plasmas **8**, 2549–2557 (2001).
[5]C. Cheon, J. Choi, J. B.-W. Koo, and J. Y. Kim, "Experimental evidence of various mode numbers of azimuthal waves in an E × B penning source for semiconductor processing," Plasma Sources Sci. Technol. **32**, 07LT01 (2023).
[6]R. Gueroult, J.-M. Rax, and N. J. Fisch, "Opportunities for plasma separation techniques in rare earth elements recycling," J. Cleaner Prod. **182**, 1060–1069 (2018).
[7]S. Zweben, R. Gueroult, and N. Fisch, "Plasma mass separation," Phys. Plasmas **25**, 090901 (2018).
[8]R. Gueroult, S. J. Zweben, N. J. Fisch, and J.-M. Rax, "E × B configurations for high-throughput plasma mass separation: An outlook on possibilities and challenges," Phys. Plasmas **26**, 04321 (2019).
[9]M. Rosenbluth, N. Krall, and N. Rostoker, "Finite larmor radius stabilization of weakly unstable confined plasmas," Technical Report No. GA2371, 1961.
[10]F. F. Chen, "Microinstability and shear stabilization of a low-β, rotating, resistive plasma," Phys. Fluids **9**, 965–981 (1966).
[11]P. Popovich, M. V. Umansky, T. A. Carter, and B. Friedman, "Modeling of plasma turbulence and transport in the large plasma device," Phys. Plasmas **17**, 122312 (2010).
[12]R. Gueroult, J.-M. Rax, and N. J. Fisch, "Centrifugal instability in the regime of fast rotation," Phys. Plasmas **24**, 082102 (2017).
[13]A. Simon, "Instability of a partially ionized plasma in crossed electric and magnetic fields," Phys. Fluids **6**, 382–388 (1963).
[14]T. K. Chu, B. Coppi, H. W. Hendel, and F. W. Perkins, "Drift instabilities in a uniformly rotating plasma cylinder," Phys. Fluids **12**, 203–208 (1969).
[15]D. B. Ilić, T. D. Rognlien, S. A. Self, and F. W. Crawford, "Low-frequency flute instabilities of a hollow cathode arc discharge: Theory and experiment," Phys. Fluids **16**, 1042–1053 (1973).
[16]T. D. Rognlien, "Low-frequency flute instabilities of a bounded plasma column," J. Appl. Phys. **44**, 3505–3512 (1973).
[17]K. Hara, A. R. Mansour, and S. Tsikata, "Theory of gradient drift instabilities in low-temperature, partially magnetised plasmas," J. Plasma Phys. **88**, 905880408 (2022).
[18]A. Smolyakov, O. Chapurin, W. Frias, O. Kosharov, I. Romadanov, T. Tang, M. Umansky, Y. Raitses, I. Kaganovich, and V. Lakhin, "Fluid theory and simulations of instabilities, turbulent transport and coherent structures in partially-magnetized plasmas of e x b discharges," Plasma Phys. Controlled Fusion **59**, 014041 (2017).
[19]G. M. Wheeler and R. V. Pyle, "Low-frequency waves in a weakly ionized, rotating magnetoplasma," Phys. Fluids **16**, 1917–1921 (1973).
[20]D. A. D'Ippolito and N. A. Krall, "Electric field driven flute instabilities in a nonuniform collisional plasma," Phys. Fluids **17**, 1848–1852 (1974).
[21]R. F. Ellis and E. Marden-Marshall, "Comparison of local and nonlocal theories of the collisional drift instability," Phys. Fluids **22**, 2137–2139 (1979).
[22]I. Romadanov, A. Smolyakov, Y. Raitses, I. Kaganovich, T. Tang, and S. Ryzhkov, "Structure of nonlocal gradient-drift instabilities in hall E x B discharges," Phys. Plasmas **23**, 122111 (2016).
[23]S. Aggarwal, Y. Camenen, A. Escarguel, and A. Poyé, "Centrifugal instability in a weakly magnetized rotating plasma column," J. Plasma Phys. **89**, 905890310 (2023).
[24]M. Matsukuma, T. Pierre, A. Escarguel, D. Guyomarc'h, G. Leclert, F. Brochard, E. Gravier, and Y. Kawai, "Spatiotemporal structure of low frequency waves in a magnetized plasma device," Phys. Lett. A **314**, 163–167 (2003).
[25]T. Pierre, A. Escarguel, D. Guyomarc'h, R. Barni, and C. Riccardi, "Radial convection of plasma structures in a turbulent rotating magnetized-plasma column," Phys. Rev. Lett. **92**, 065004 (2004).
[26]R. Barni, C. Riccardi, T. Pierre, G. Leclert, A. Escarguel, D. Guyomarc'h, and K. Quotb, "Formation of spiral structures and radial convection in the edge region of a magnetized rotating plasma," New J. Phys. **7**, 225 (2005).
[27]F. Brochard, E. Gravier, and G. Bonhomme, "Transition from flute modes to drift waves in a magnetized plasma column," Phys. Plasmas **12**, 062104 (2005).
[28]S. Jaeger, T. Pierre, and C. Rebont, "Direct observation of a cross-field current-carrying plasma rotating around an unstable magnetized plasma column," Phys. Plasmas **16**, 022304 (2009).
[29]A. Escarguel, "Optical diagnostics of a low-frequency instability rotating around a magnetized plasma column," Eur. Phys. J. D **56**, 209–214 (2010).
[30]S. Aggarwal, "Linear stability of a weakly magnetized rotating plasma column," Ph.D. thesis (Aix-Marseille University, 2023).

[31]S. I. Braginskii, "Transport processes in a plasma," Rev. Plasma Phys. **1**, 205 (1965).
[32]J. J. Ramos, "General expression of the gyroviscous force," Phys. Plasmas **12**, 112301 (2005).
[33]B. M. Annaratone, A. Escarguel, T. Lefevre, C. Rebont, N. Claire, and F. Doveil, "Rotation of a magnetized plasma," Phys. Plasmas **18**, 032108 (2011).
[34]C. Rebont, "Etude d'une colonne de plasma magnetise par fluorescence induite par laser," Ph.D. thesis (Aix-Marseille University, 2010).
[35]S. Jaeger, "Étude théorique et exp érimentale des instabilités basses fréquences dans un plasma en champs magnétique et éléctrique croisés," Ph.D. thesis (Université de Provence, 2010).
[36]P. David, "Tomography in a linear magnetised plasma," Ph.D. thesis (Aix-Marseille Université, 2017).
[37]J. Rax, A. Fruchtman, R. Gueroult, and N. Fisch, "Breakdown of the Brillouin limit and classical fluxes in rotating collisional plasmas," Phys. Plasmas **22**, 092101 (2015).
[38]F. C. Hoh, "Simple picture of the finite Larmor radius stabilization effect," Phys. Fluids **6**, 1359–1359 (1963).
[39]A. V. Phelps, "The application of scattering cross sections to ion flux models in discharge sheaths," J. Appl. Phys. **76**, 747–753 (1994).
[40]J. Vlcek, "A collisional-radiative model applicable to argon discharges over a wide range of conditions. I. Formulation and basic data," J. Phys. D: Appl. Phys. **22**, 623 (1989).
[41]R. B. White, *Asymptotic Analysis of Differential Equations* (Imperial College Press, New York, 2005).